Gallium-Based Room Temperature Liquid Metals and its Application to Single Channel Two-Liquid Hyperelastic Capacitive Strain Sensors

by

Shanliangzi Liu

A Thesis Presented in Partial Fulfillment
of the Requirements for the Degree
Master of Science

Approved April 2015 by the
Graduate Supervisory Committee:

Konrad Rykaczewski, Chair
Owen Hildreth
Terry Alford
Marcus Herrmann

ARIZONA STATE UNIVERSITY

May 2015

ABSTRACT

Gallium-based liquid metals are of interest for a variety of applications including flexible electronics, soft robotics, and biomedical devices. Still, nano- to microscale device fabrication with these materials is challenging because of their strong adhesion to a majority of substrates. This unusual high adhesion is attributed to the formation of a thin oxide shell; however, its role in the adhesion process has not yet been established. In the first part of the thesis, we described a multiscale study aiming at understanding the fundamental mechanisms governing wetting and adhesion of gallium-based liquid metals. In particular, macroscale dynamic contact angle measurements were coupled with Scanning Electron Microscope (SEM) imaging to relate macroscopic drop adhesion to morphology of the liquid metal-surface interface. In addition, room temperature liquid-metal microfluidic devices are also attractive systems for hyperelastic strain sensing. Currently two types of liquid metal-based strain sensors exist for inplane measurements: single-microchannel resistive and two-microchannel capacitive devices. However, with a winding serpentine channel geometry, these sensors typically have a footprint of about a square centimeter, limiting the number of sensors that can be embedded into. In the second part of the thesis, firstly, simulations and an experimental setup consisting of two GaInSn filled tubes submerged within a dielectric liquid bath are used to quantify the effects of the cylindrical electrode geometry including diameter, spacing, and meniscus shape as well as dielectric constant of the insulating liquid and the presence of tubing on the overall system's capacitance. Furthermore, a procedure for fabricating the two-liquid capacitor within a single straight polydiemethylsiloxane channel is developed. Lastly,

capacitance and response of this compact device to strain and operational issues arising from complex hydrodynamics near liquid-liquid and liquid-elastomer interfaces are described.

DEDICATION

The thesis is dedicated to my parents who supported me financially and spiritually during my study in Arizona State University.

I would also like to thank my sister who were always there cheering me up and giving me best suggestions.

Finally, I would like to give thanks to my fiancé for loving me and encouraging me to reach my dream.

ACKNOWLEDGEMENTS

First of all, I would like to express my sincere gratitude to my supervisor Dr. Rykaczewski for his patience, enthusiasum and immense knowledge through the research work of my master thesis. The thesis would not have been possible without the guidance of him.

I would also like to thank my committee members: Dr. Hildreth, Dr. Herrmann and Dr. Alford for their insightful comments, remarks and encouragement.

Furthermore, I am grateful to Dr. Doudrick from the University of Notre Dame for his meticulous guidance on the first part of my thesis work and his perspective comments on my paperwork.

My sincere thanks also go to my fellow labmates in Dr. Rykaczewski's research group: Xiaoda Sun and Viraj Damle for providing useful suggestions and cooperation.

Last but not the least, I would like to thank the startup funding from Fulton School of Engineering at Arizona State University for financially supporting my research.

TABLE OF CONTENTS

Page

LIST OF FIGURES

FIGURE Page

FIGURE Page

LIST OF TABLES

TABLE Page

INTRODUCTION

Stretchable electronic components have a variety of applications including flexible electronics, biomedical devices, and soft robotics.(Cheng & Wu, 2010; D.-H. Kim & Rogers, 2008; J. Park et al., 2012a; Rogers, Someya, & Huang, 2010) Room-temperature liquid metals are particularly attractive for fabrication of such devices because in contrast to conventional semiconductor based stretchable electronics, (Feng et al., 2011; D.-H. Kim & Rogers, 2008) circuits and sensors comprising of these materials are intrinsically soft and can retain their functionality even when stretched to several times their original length. (Cheng & Wu, 2012) One of the earliest examples of liquid-phase electronics is the Whitney strain gauge, (WHITNEY, 1949) which measures strain of a mercury-filled rubber tube by measuring variation in electric resistance of the metal due to change in its geometry. In the last two decades mercury and rubber have been replaced by non-toxic liquid gallium alloys such as gallium-indium (GaIn) or gallium-indium-tin (GaInSn also known as Galinstan) and more elastic Polydiemethylsiloxane (PDMS). Gallium-based liquid metals have been proposed for a number of applications including strain or curvature sensors, (Cheng & Wu, 2011; R.K. Kramer, Majidi, Sahai, & Wood, 2011; R.K. Kramer, Majidi, & Wood, 2011; Majidi, Kramer, & Wood, 2011; Noda, Iwase, Matsumoto, & Shimoyama, 2010; Y.-L. Park, Majidi, Kramer, Bérard, & Wood, 2010) stretchable circuits and antennas, (Cheng, Rydberg, Hjort, & Wu, 2009; Cheng, Wu, Hallbjorner, Hjort, & Rydberg, 2009; Cumby et al., 2012; Jalali Mazlouman, Jiang, Mahanfar, Menon, & Vaughan, 2011; Koo, So, Dickey, & Velev, 2011; Kubo et al., 2010; Paik, Kramer, & Wood, 2011; Palleau, Reece, Desai, Smith, & Dickey, 2013; So et al., 2009) microelectronic heat sinks, (Haiyan Li, n.d.; Kunquan Ma, 2007; Lam, Hodes,

& Enright, 2013; Ma & Liu, 2007; Vetrovec, Litt, Copeland, Junghans, & Durkee, 2013) thermal interface materials, (Zhang & Liu, 2013) electrical interconnects and contacts, (Cao, Yuen, & Lin, 2007; H.-J. Kim, Maleki, Wei, & Ziaie, 2009; H.-J. Kim, Son, & Ziaie, 2008) droplet-based micro-switches, (Wenjiang Shen, 2006) micro-syringes for cells,(Knoblauch, Hibberd, Gray, & van Bel, 1999) radio-frequency switches, (P. Sen, 2009) resonators, (M.R. Khan, Hayes, Zhang, Dickey, & Lazzi, 2012) tunable aplasmonics, (Wang, Liu, Vardeny, & Nahata, 2012) actuators, (Finkenauer & Majidi, 2014; S.-Y. Tang et al., 2014) transmission lines, (Hayes et al., 2014) and tunable-frequency selective surfaces. (M. Li, Yu, & Behdad, 2010)

Because of this wide application scope, several new methods of fabricating gallium-based liquid metal structures have been proposed. The recent alternatives include using direct writing, (Boley, White, Chiu, & Kramer, 2014; Gao, Li, & Liu, 2012, 2013) vacuum-induced patterning, (Cumby et al., 2012; J. Park et al., 2012b) contact printing, (Jeong et al., 2012a; Tabatabai, Fassler, Usiak, & Majidi, 2013; Wissman, Lu, & Majidi, 2013) roller-ball pen, (Zheng, He, Yang, & Liu, 2013; Zheng, Zhang, & Liu, 2013) masked deposition, (Rebecca K. Kramer, Majidi, & Wood, 2013) micro-fluidic flow focusing, (Thelen, Dickey, & Ward, 2012) co-electro-spinning, (H. Yang, Lightner, & Dong, 2011) freeze-casting, (Andrew Fassler & Majidi, 2013) airbrushing, (Zhang, Gao, & Liu, 2013) and 3D printing. (Ladd, So, Muth, & Dickey, 2013; Trlica, Parekh, Panich, Ladd, & Dickey, 2014) However, fabrication of well-defined geometrical features with sizes significantly below 5 μm has proven to be difficult.

The limited spatial resolution is attributed to complex rheology and wetting of the liquid metals (Dickey et al., 2008; D. Kim, Thissen, et al., 2013; Rebecca K. Kramer,

Boley, Stone, Weaver, & Wood, 2013; T. Liu, Sen, & Kim, 2010, 2012) caused by the thin oxide skin that rapidly forms when these liquids are exposed to an oxygen concentration above 1 ppm (T. Liu et al., 2010, 2012; V. Sivan et al., 2013) (or in other reports, a dose of $1.8x10^{-4}$ Torr-s). (Regan, Pershan, et al., 1997; Regan, Tostmann, et al., 1997) Although the surface composition of GaIn and GaInSn is dominated by indium, (Dickey et al., 2008; Dumke, Tombrello, Weller, Housley, & Cirlin, 1983) the oxide shell of both alloys primarily consists of Ga_2O_3 because it oxides rapidly and is thermodynamically preferred over In_2O_3. (Dickey et al., 2008; Dumke et al., 1983; D. Kim, Thissen, et al., 2013) Also, despite a thickness of only 0.5 to 2.5 nm, (Dickey et al., 2008; Dumke et al., 1983; Regan, Pershan, et al., 1997; Regan, Tostmann, et al., 1997; Scharmann et al., 2004) this thin film is robust enough to mechanically stabilize the structure, (Ladd et al., 2013) which leads to macroscopic viscoelastic behavior of the liquid metals in the presence of air until the critical surface yield stress (about 0.5 N/m) (Dickey et al., 2008; Scharmann et al., 2004) is exceeded. The oxide shell has also been reported to strongly adhere to almost any surface, (D. Kim, Lee, Choi, & Lee, 2013; Scharmann et al., 2004) making manipulation and transfer of the liquid metals challenging. Several routes of mitigating the high adhesion of the oxide including embedding of metal droplets in hydrophobic nanoparticles (i.e., liquid marbles), (V. Sivan et al., 2013; S.-Y. Tang et al., 2013; X. Tang et al., 2013; S. Y. T. V. Sivan, 2012) use of textured metal-phobic surfaces, (D. Kim, Lee, Choi, et al., 2013) hydrochloric acid liquid or vapor treatment, (Dickey et al., 2008; D. Kim, Thissen, et al., 2013) and acid-impregnated surfaces (D. Kim, Lee, Lee, Choi, & Lee, 2013; G. Li, Parmar, Kim, Lee, & Lee, 2014) are been proposed. However, thus far, none of these methods have aided to increase the

patterning spatial resolution of GaIn and GaInSn. A better understanding of the phenomena underlying the liquid metal adhesion and wetting behaviours could lead to improved fabrication methods with higher spatial resolution. To this end, the first part of this thesis describes a multiscale study aiming at understanding the fundamental mechanisms governing wetting and adhesion of gallium-based liquid metals. In particular, macroscale dynamic contact angle measurements were coupled with Scanning Electron Microscope (SEM) imaging to relate macroscopic drop adhesion to morphology of the liquid metal-surface interface.(Doudrick et al., 2014)

The second part of this thesis focuses on development of a novel single channel liquid metal-liquid dielectric hyperelastic capacitative strain sensor. This type of device is proposed as an alternative to resistive liquid metal strain sensor. While popular and robust, these sensors have a large footprint limits the areal density that they can be embedded into a wearable electronic skin. For example a ~1 Ω resistor made out of GaInSn with resistivity of 0.29 μΩm in a 200 μm diameter channel has a length of ~10 cm. By winding the channel 10 times such sensor can be fit into an area of ~1 cm^2. Improved understanding of the GaIn and GaInSn wetting characteristics (Dickey et al., 2008; D. Kim, Thissen, et al., 2013; Rebecca K. Kramer, Boley, et al., 2013; T. Liu et al., 2010, 2012) and advances in their micro-fabrication (Boley et al., 2014; Cumby et al., 2012; Gao et al., 2012, 2013; Jeong et al., 2012b; Rebecca K. Kramer, Boley, et al., 2013; Rebecca K. Kramer, Majidi, et al., 2013; Ladd et al., 2013; J. Park et al., 2012b; Thelen et al., 2012; Wissman et al., 2013; H. Yang et al., 2011; Z. Yang, Deng, Chen, Ren, & Peng, 2013; Zheng, He, et al., 2013) are enabling fabrication of smaller liquid metal filled microchannels with higher areal density; however, the required serpentine geometry of these resistors remains quite complex.

Several designs of capacitive strain sensors have been proposed as alternatives to the resistive devices. (A. Fassler & Majidi, 2013; Ponce Wong, Posner, & Santos, 2012) These capacitive devices consist of two microchannels filled with liquid metal separated by the dielectric PDMS matrix (see schematic in Figure 1.1a). For in-plane sensing an order of magnitude estimate for the required sensor footprint can be obtained using the parallel plate capacitor model, $C \approx \varepsilon_0 \varepsilon A/d$ (i.e. $A \approx Cd/\varepsilon_0 \varepsilon$). To achieve a capacitance (C) of ~1 pF, two liquid metal-filled microchannels with both height (h) and separation (d) of ~400 μm within a PDMS matrix (ε~2) must have a length of l~10 cm (from conductor-dielectric interfacial area, $A \sim lh$~4x10^{-5} m2). By winding the parallel channels in a serpentine arrangement, such a sensor can fit within a base area of several square centimeters. Fassel and Majidi (A. Fassler & Majidi, 2013) recently showed that such base area is required for a variety of winding two-channel capacitive strain sensor designs to achieve C~1-15 pF. With such a large footprint the sensor output is affected by stretching in multiple directions, not only in the desired principle direction. As a result, correlation of the physical strain with the sensor output is complex. (A. Fassler & Majidi, 2013)

Since parallel plate capacitance is proportional to both the conductor-dielectric interfacial area and the dielectric constant, a decrease in the required length of the parallel channels, and with that the sensor footprint, should be achievable by increasing the dielectric constant of the insulator material. While solid elastomers with ε greater than that of PDMS (ε~2) are not readily available, common liquids like glycerol and water have ε~40 and ε~80, respectively. According to the parallel plate model scaling, replacing PDMS with these dielectric liquids would decrease the

required conductor-dielectric interfacial area of a sensor by 20 to 40 times. (S. Liu et al., 2015)

To this end, the second part of this thesis explores the concept of a capacitor composed of two liquid metal electrodes separated by a liquid dielectric within a single straight cylindrical microchannel (see schematic in Figure 1.1b). Simulations and an experimental setup consisting of two GaInSn filled tubes submerged within a dielectric liquid bath are used to quantify the effects of the cylindrical electrode geometry including diameter, spacing, and meniscus shape as well as dielectric constant of the insulating liquid and the presence of tubing on the overall system's capacitance. Next, a procedure for fabricating the two-liquid capacitor within a single straight cylindrical PDMS channel is developed. Lastly, capacitance and response of this compact device to strain and operational issues arising from complex hydrodynamics near liquid-liquid and liquid-elastomer interfaces are described.

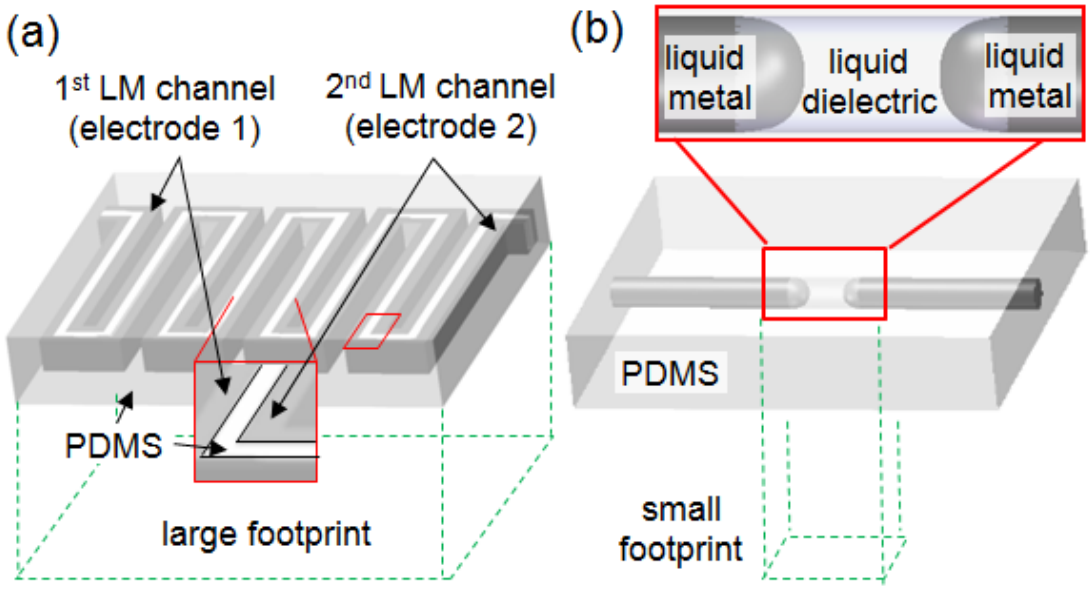

Figure 1.1 Schematic comparison of capacitor geometries comprising of (a) two winding liquid metal filled channels separated by solid elastomer and (b) single channel filled with liquid metal and liquid dielectric.

GALLIUM-BASED LIQUID METALS

Liquid metal consists of alloys with low melting points, which are in liquid phase at room temperature. (D. Kim, Thissen, et al., 2013) Mercury is the most common type of liquid metal, which has formerly been used in thermometers, sphygmomanometers, and dental amalgams. (Dickey, 2014) ("Mercury (element)," 2015) However, mercury is toxic and it has a large surface tension which limits it to spherical shapes. Recently, Gallium-based liquid alloys such as gallium-indium (GaIn) or gallium-indium-tin (GaInSn also known as Galinstan) have been evaluated as promising replacements for mercury due to their low toxicity and other favourable properties. ("Microsoft Word - MSDS_Galinstan engl. 03_18_04 .doc - msds.pdf," n.d.) In this chapter, physical properties and wetting and adhesion behaviours of gallium-based liquid metals will be introduced. This summary will illustrate the advantages of gallium-based liquid alloys in the application of stretchable sensors or biomedical devices.

Compositions and physical properties

Two most common room temperature gallium liquid alloys are galinstan and eGaIn. Galinstan is a nearly eutectic alloy of gallium (Ga), indium (In), and tin(Sn), and its name is made of the three components (-stan referring to tin). ("Galinstan - Wikipedia, the free encyclopedia," n.d.) Typical eutectic composition of galinstan is 68 wt% Ga, 22 wt% In and 10 wt% Sn, with a melting temperature of −19 °C (−2 °F). (Cheng & Wu, 2012) EGaIn is a similar eutectic liquid metal, but it is only composed of 75.5 wt% Ga and 24.5 wt% In, with a melting temperature of 15.5 °C (60 °F).

In contrast to majority of metals, galinstan and eGaIn remain in liquid state at room temperature and have a low-viscosity in the absence of the oxide skin

(approximately two times of water). (Spells, 1936) When a critical pressure is applied to the inlet of a channel in a microfluidic device, the liquid metal will rapidly flow into and fill the microchannels at room temperature. (Dickey et al., 2008) Compared with ordinary electrolyte solutions, liquid metals have advantages of inherent high densities and surface tension, as well as excellent electrical and thermal conductivities. Physical properties of galinstan, EGaIn, and mercury are compared in Table 2.1.

Table 2.1

Comparison of physical properties of galinstan, EGaIn, and mercury. (Morley, Burris, Cadwallader, & Nornberg, 2008)

	Galinstan	EGaIn	Hg
Melting point (℃)	-19	15.5	-38.8
Boiling point (℃)	>1300	2000	1353
Density($kg \cdot m^{-3}$)	6440	6280	357
Electrical conductivity($S \cdot m^{-1}$)	$3.46x10^{6}$	$3.4x10^{6}$	$1.0x10^{6}$
viscosity ($Pa \cdot s$)	$2.4x10^{-3}$	$2.0x10^{-3}$	$1.5x10^{-3}$
surface tension ($N \cdot m^{-1}$)	0.718	0.624	0.487

When exposed to an oxygen concentration above 1 ppm (T. Liu et al., 2010, 2012; V. Sivan et al., 2013), a passivating oxide layer rapidly forms on surface of all gallium based liquid metals, just as in the case of aluminum. But the oxide skin grows only to 1-2 nm thickness and thus does not significantly alter thermal or electrical properties of the metal. (Regan, Tostmann, et al., 1997) More importantly, despite the effect of low viscosity and large surface tension, the passivating oxide skin mechanically stabilizes non-equilibrium microstructures. (Dickey et al., 2008; Ladd et al., 2013) In contrast, the metal tends to bead up to minimize the interfacial tension in the absence

of the skin. (D ZRNIC, 1969) All these properties make room temperature liquid metals potential candidates in the applications of microfluidic electronic devices.

Wetting and adhesion behaviours

Room temperature liquid metals are promising components for novel microfluidic electronic devices. Previously, these devices were fabricated by producing silicone elastomers mold by casting, sealing with a thin layer of the same material and then injecting liquid metals into the mold with a syringe needle. (Rebecca K. Kramer, Majidi, et al., 2013) However, due to the manual and complicated nature of the process, limited possible device geometry and difficulty of realizing mass-producing, this method is gradually being replaced by alternatives such as contact printing, (Jeong et al., 2012a; Tabatabai et al., 2013; Wissman et al., 2013) masked deposition, (Rebecca K. Kramer, Majidi, et al., 2013) and 3D printing. (Ladd et al., 2013; Trlica et al., 2014) etc. Still, nano- to microscale device fabrication with these materials is challenging because, despite having surface tension (see table 2.1) 10 times higher than water, they strongly adhere to a majority of substrates. This unusually high adhesion is attributed to the formation of a thin oxide shell; however, its role in the adhesion process has not yet been established. Therefore, the wetting and adhesive behaviors of Gallium-based liquid metals on different surfaces, especially the drop-substrates interactions caused by the oxide shell rapidly formed on liquid metals play an important role in the improvement of spatial resolution in liquid metal printing processes.

In this chapter, the concept of wetting and adhesive phenomenon, work of adhesion, contact angle hysteresis and measuring methods are introduced. In addition, measurement of macro-scale dynamic contact angle of liquid metals on variety of

surfaces are described. (Antoniou, Rykaczewski, & Uchic, 2014) Based on the results of these experiments, a new theory for the fundamental mechanisms governing liquid metals interaction with different substrates is proposed.

Concept of wetting, adhesive forces and contact angle. Wetting is the ability of a liquid to form interface with a solid or liquid substrate due to intermolecular interactions between them. Wettability of material 1 on material 2 is determined by the resultant of adhesive forces and cohesive forces between two materials. ("Wetting," 2015) Adhesion is the tendency of two media to stick to one another, while cohesion is the tendency of the same medium to remain united. ("Adhesion," 2015) Work of adhesion and cohesion are defined to study the processes involving the contact between an object and a substrate. As shown in the Figure 2.1, the work of adhesion in a third medium is defined as W132 , which is the energy needed to separate two species 1 and 2 in a dissimilar media 3. (Israelachvili, 2011) The equation can be expressed as:

$$W_{132} = W_{12} + W_{33} - W_{13} - W_{23} = \gamma_{13} + \gamma_{23} - \gamma_{12} \quad (2.1)$$

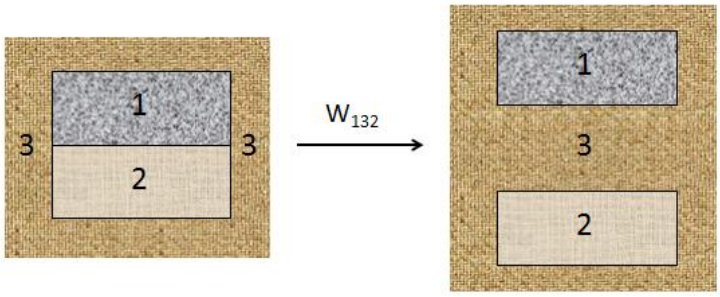

Figure 2.1 Schematic of the work of adhesion of two dissimilar surfaces in a third medium.

According to the Johnson, Kendall, and Roberts theory, (Johnson, Kendall, & Roberts, 1971) the adhesion force (i.e., pull-off, separation force) between a sphere of

species 2 with radius R and a flat substrate of material 1 in the presence of medium 3 can be expressed as (Israelachvili, 2011)

$$F_{ad} = -\frac{3}{2}\pi R W_{132} \tag{2.2}$$

which means the sphere could be separated from the substrate when the pull-off force reaches the adhesion force F_{ad}. When adhesive forces between a liquid sphere and a solid substrate are greater than cohesive forces, the liquid drop tends to spread on the surface, which is the phenomenon of total wetting or partial wetting. Inversely, if cohesive forces are greater, the liquid drop tends to collect into a ball, reducing the area in contact with the surface. The liquid drop is dewetting (non-wetting) the surface in this situation.

The JKR theory (Israelachvili, 2011) was derived based on perfectly smooth surfaces. However, most surfaces have roughness, which may affect adhesion forces. According to recent experiments by Benz et al. (Benz, Rosenberg, Kramer, & Israelachvili, 2006) and Zappone et al. (Zappone, Rosenberg, & Israelachvili, 2007) and modeling by Yang et al. (C. Yang, Persson, Israelachvili, & Rosenberg, 2008), the adhesive force

$$F_{ad}(\varepsilon) = F_{ad}(0)e^{-\varepsilon_{rms}/\varepsilon_0} \tag{2.3}$$

where ε_{rms} is the roughness of the surface, $F_{ad}(0)$ is the adhesion force on a flat surface ($\varepsilon = 0$), ε_0 is a constant. (Israelachvili, 2011) Because of the exponential nature of the upper equation, even roughness on the order of a few nanometers can significantly lower the adhesion force.

The wettability of media 1 on media 2 in media 3 could be represented institutively by contact angle, which is a good indicator of adhesive and cohesive

forces. As shown in Figure 2.2, contact angle is the angle a liquid drop creates when a liquid/vapor interface meets a liquid/solid surface. (“Contact Angles,” n.d.) Contact angle is a measurable quantity and it is in an inverse relation with wettability. When adhesive forces dominate in the interaction between a sphere and a substrate, molecules of a liquid drop tend to interact more with the substrate rather than their similar liquid molecules. (“Contact Angles,” n.d.) In this case, liquid drop deposited on the surface tends to spread out, forming a contact angle less than 90 °. Low contact angle is an indicator of favourable wettability. A liquid perfectly wets a substrate when contact angle on the interface is nearly 0 °. In contrast, when cohesive forces dominate, liquid molecules are more inclined to interact with each other, so they form contact angle larger than 90 °on a surface. A liquid perfectly non-wetting (de-wetting) a surface is indicated by a contact angle nearly 180 °. The liquid drop is almost not contacting with the substrate in this case.

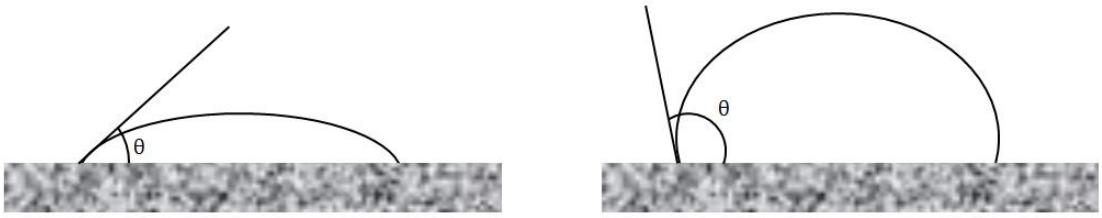

Figure 2.2 Schematic of different liquids wetting a surface showing contact angle.

The shape of a liquid deposited on a surface within a vapor phase could be expressed as the a relation of equilibrium contact angle θ, solid-vapor interfacial tension γ_{SV}, solid-liquid interfacial tension γ_{SL}, and liquid-vapor interfacial tension (surface tension) γ_{LV}, which is called Young’s equation. (Chow, 1998) (see Figure 2.3 and eq 2.4)

$$\gamma_{SV} - \gamma_{SL} = \gamma_{LV} cos\theta \quad (2.4)$$

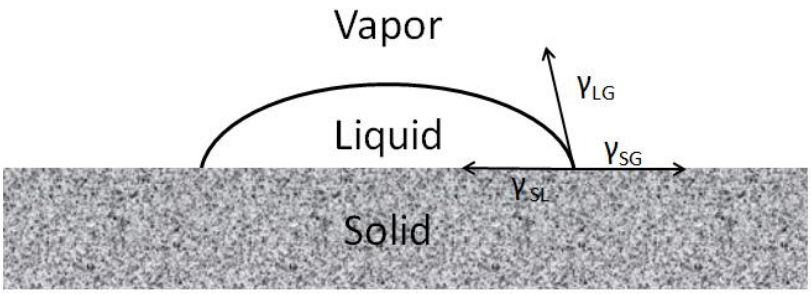

Figure 2.3 Schematic of a liquid drop on a solid substrate showing Young's equation.

Contact angle hysteresis. One could expect the contact angle to be an unique value, but in practice, multiple values for the contact angle can be observed. This phenomenon is due to imperfections of surfaces. Although most surfaces seem flat, they have roughness or contaminants that cannot be seen by naked eyes. Therefore, if small amount of liquid is added to the drop deposited on a substrate, the volume of the drop increases while the contact line is pinned on the defects. As a result the contact angle increases until the contact area starts to advance. This threshold largest dynamic contact angle is called the advancing contact angle θ_A. Conversely, if small amount of liquid is withdrawn from the drop, the volume of the drop while the contact area is maintained until it begins to recedes. The contact angle at which the contact line begins to move is called the receding contact angle θ_R. The difference between $\theta_A - \theta_R$ is termed as contact angle hysteresis. (Quéré, 2005) In Young's equation, the surface is assumed to be perfectly flat, so θ is an equilibrium contact angle between advancing and receding contact angles, ("Contact angle," 2015) which can be calculated from θ_A and θ_R by the equation derived by Tadmor (Tadmor, 2004) and experimentally verified by Chibowski (Chibowski & Terpilowski, 2008) as ("Contact angle," 2015):

$$\theta = \arccos\left(\frac{\gamma_A \cos\theta_A + \gamma_R \cos\theta_R}{\gamma_A + \gamma_R}\right) \quad (2.5)$$

where $\gamma_A = \left(\frac{\sin^3\theta_A}{2 - 3\cos\theta_A + \cos^3\theta_A}\right)^{1/3}$; $\gamma_R = \left(\frac{\sin^3\theta_R}{2 - 3\cos\theta_R + \cos^3\theta_R}\right)^{1/3}$

Static and dynamic contact angle measurement. The static contact angles are measured when the droplet is sitting on the surface and the contact area is kept static. In this case, contact angle goniometer with an optical system or a high resolution/speed camera are usually used to capture the image of liquid drop standing on a solid substrate. ("zafepress.php," n.d.) Contact angles could be directly measured and analyzed from those images. Dynamic contact angle are measured by adding and later reducing volume of a liquid in contact with a surface. This way advancing and receding contact angles and contact angle hysteresis can be acquired. ("Contact angle," 2015)

Macroscale dynamic contact angle measurements—volume variation method (VV) and height variation method (HV). (Doudrick et al., 2014) First, macroscale dynamic contact angle measurements were performed to acquire contact angle hysteresis and to understand the fundamental mechanisms governing wetting and adhesion behaviours of gallium-based liquid metals. To study the impact of the oxide shell on GaInSn adhesion, the liquid metal's advancing contact angle θ_A and receding contact angle θ_R on variety of surfaces were measured using two methods. Schematic apparatus that was used to measure dynamic contact angles are shown in Figure 2.4.

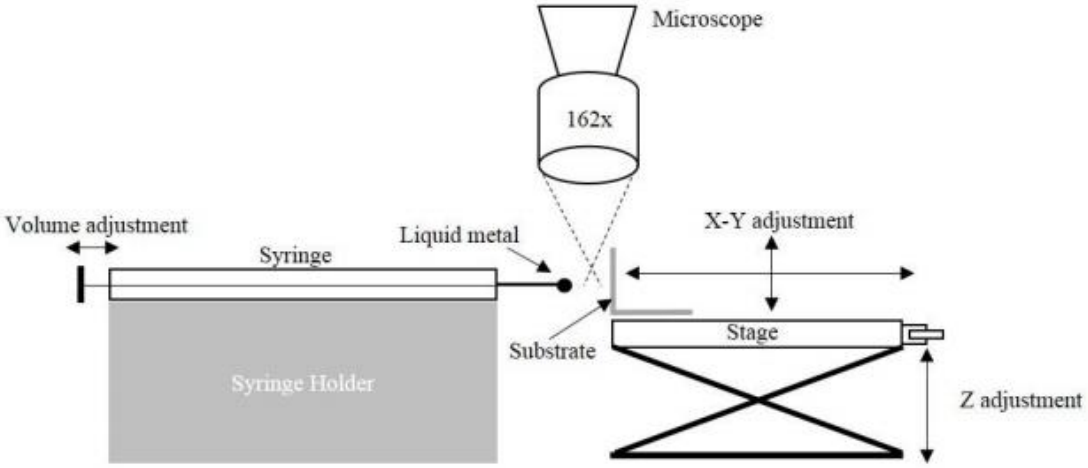

Figure 2.4 Schematic of the custom apparatus used for dynamic contact angle measurements.

In the first approach, the position of the surface was fixed while the volume of the liquid metal drop forming at tip of a syringe was varied. Specifically, the volume was increased as drop made contact with and expanded over the surface and subsequently decreased until the drop retracted from the surface (see Figure 2.5a). This approach, which is referred to as the volume variation method (VV), is commonly used to measure the contact angle hysteresis (CAH) of liquids on solid substrates. (Gennes, Brochard-Wyart, & Quere, 2004) Increasing the GaInSn volume creates new surface area and leads to exposure of bare liquid metal followed by initiation of new oxide growth within microfractures of the old oxide shell. Thus, the CAH measured using the volume variation method is a measure of the adhesion of the composite interface that includes oxide of various ages and potentially bare liquid metal on variety of substrates. To probe the adhesive properties of GaInSn without rupturing of the oxide skin, an alternative approach was developed, which is referred to as the height variation method (HV). In this second approach, to avoid breaking the oxide shell, the sample surface was gently brought in contact with and retracted from a liquid metal drop having a fixed volume. Thus, the CAH measured using this approach quantifies

the adhesion between the substrate and surface of the unbroken oxide (i.e., exposure of bare liquid metal followed by oxide regrowth is minimized). Advancing and receding angle of GaInSn on glass, tungsten, PTFE and PDMS surfaces were measured using both volume (VV) and substrate height variation (HV) methods. Optical images sequences are illustrated in Figure 2.5. Contact angle measurements are shown in Table 2.2. In addition, to ensure that the second approach was applicable to measuring of dynamic contact angles, the CAH of water on OTS (Octadecyltrichlorosilane) coated silicon wafer (a flat hydrophobic surface) was measured using both approaches. Values in Table 2.2 show that a close match for advancing and receding contact angles was obtained.

Figure 2.5 Optical images of advancing and receding contact angles of GaInSn on (a, b) glass, (c) tungsten, (d) PTFE, and (e) PDMS surfaces measured using volume (VV) and substrate height variation (HV) methods in air at about 98 kPa. The scale bar corresponds to 230 μm.

Table 2.2

Advancing (θ_A) and receding (θ_R) contact angles measurements with corresponding standard deviation (σ). All values are in degrees.

	surface height variation method				**drop volume variation method**			
liquid/surface	θ_A	$\sigma_{\theta A}$	θ_R	$\sigma_{\theta R}$	θ_A	$\sigma_{\theta A}$	θ_R	$\sigma_{\theta R}$
H_2O/silicon (OTS)	104.6	1.8	91.2	0.7	105.0	1.3	91.9	2.6
GaInSn/SiO_2	133.3	5.4	124.9	3.0	131.5	1.5	46.2	1.3
GaInSn/W	139.6	3.6	132.7	3.1	128.3	1.8	38.4	9.8
GaInSn/PTFE	146.0	2.4	137.6	2.3	141.2	2.7	69.3	12.3
GaInSn/PDMS	127.6	7.6	78.6	5.7	141.1	2.8	73.4	2.0
GaInSn/silicon (OTS)	140.5	5.8	121.2	7.7	146.9	3.5	49.1	3.6

Contrasting of images shown in Figure 2.5a,b reveals that dramatically different receding contact angles of GaInSn are measured on a glass substrate using the two methods. While the θ_R measured using the height variation approach is about 125 ° (CAH of 8 °), the θ_R measured by reducing droplet volume is only about 46 ° (CAH of 85 °). A nearly identical trend are observed for tungsten foil (Figure 2.5c) and polytetrafluoroethylene surfaces (PTFE; Figure 2.5d). Only the receding contact angles of GaInSn measured on polydimethylsiloxane (PDMS) are in close agreement with about 78.6 ° (CAH 49.0 °) and 73.4 ° (CAH 67.7 °) measured using the volume and height variation methods, respectively. Thus, with exception of the highly viscoelastic PDMS, the interfacial adhesion between the old, unruptured oxide and the studied flat surfaces observed using the sample height variation method is low. In this case the surface energy of the substrate, γ, does not play a significant role (γ_{PTFE} = 18 mJ/m^2, γ_{PDMS} = 19.8 mJ/m^2, γ_{SiO2} = 593 mJ/m^2, $\gamma_{W(110)}$ = 3320 mJ/m^2). (Takadoum, 2013) In contrast, exposure of bare GaInSn followed by oxidation resulting from old oxide shell rupturing during the volume addition method led to very high adhesion to all examined surfaces.

Fundamental mechanisms governing wetting and adhesion behaviours of Gallium-based liquid metals. (Doudrick et al., 2014) Based on the CAH experiments, a hypothesis that the liquid metal adhesion to flat surfaces is dominated by morphology and dynamics of formation of the oxide−surface interface is proposed. Consequently, adhesion of liquid metal to flat surfaces can occur in two modes. The schematic in Figure 2.6a illustrates the first mode that occurs during the height variation experiments and leads to formation of a solid− solid rather than solid−liquid interface.

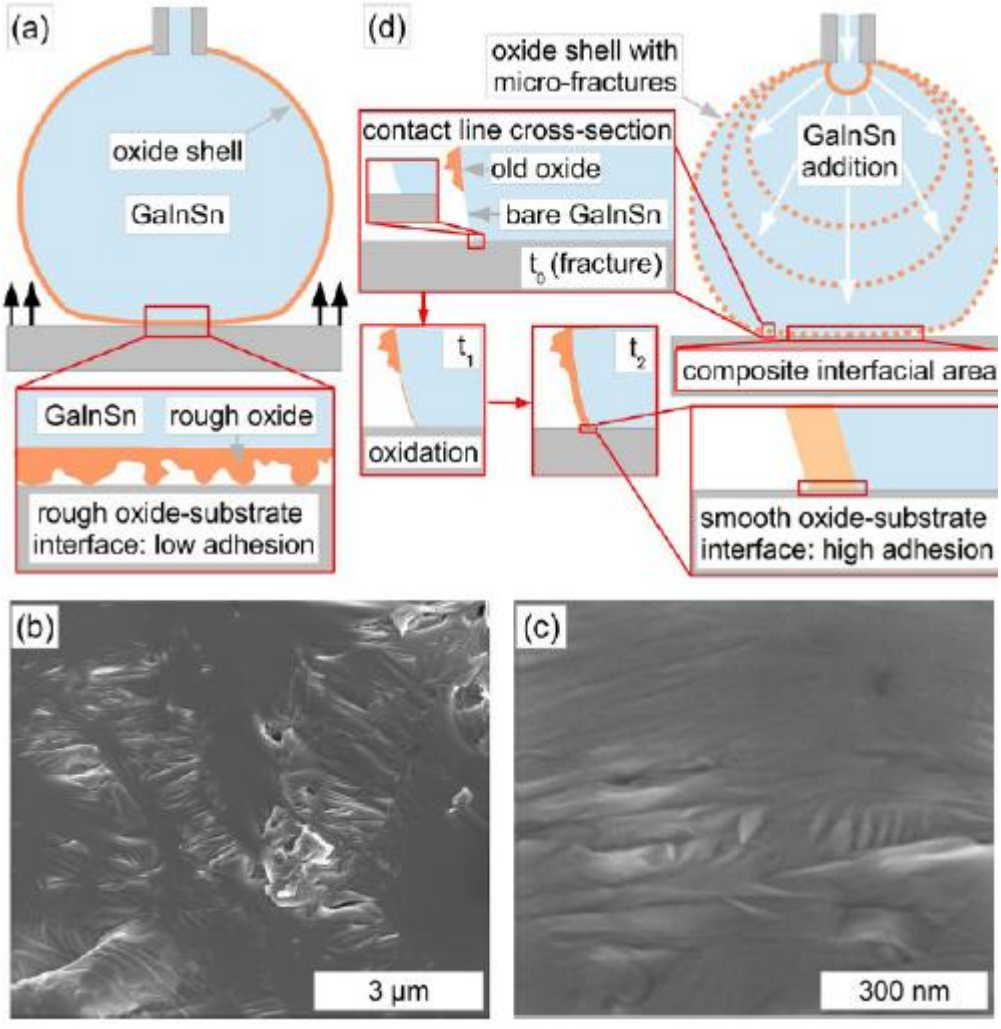

Figure 2.6 (a) Schematic illustration of the rough oxide-surface interface responsible for low adhesion measured using the height variation method and SEM images showing (b) microscale and (c) nanoscale roughness of the old, air-formed, top

surface of an oxidized GaInSn drop formed at tip of a syringe (the drop was lightly sheared across a silicon wafer to adhere for imaging). (d) Schematic illustration of the smooth oxide-surface interface formation around perimeter of drops formed using the volume addition method (a composite interfacial area consisting of fractured pieces of old oxide, new oxide, and bare GaInSn is likely present underneath the drop).

The adhesion force of two involved solids with a surface roughness is shown in equation 2.3. The SEM images in Figure 2.6b,c clearly show microscale and nanoscale roughness of the old oxide shell formed on the surface of a GaInSn drop. Thus, the low CAH measured for mode 1 using the height variation method is probably due to the old oxide roughness (eq 2.3), not inherently low work of adhesion between gallium oxide and the studied solid surfaces (eq 2.2).

An understanding of the mechanisms causing the high CAH in the second mode measured using the volume variation approach is more difficult because of the composite nature of the liquid metal−surface interfacial area and its perimeter (contact line). As the GaInSn expands over the substrate, multiple microfractures within the old oxide shell continually expose bare GaInSn. This adhesion mode was studied in detail using in situ nanoscale imaging within a Focused Ion Beam Scanning Electron Microscope (FIB-SEM) by Doudrick et al. Their conclusion was that much stronger adhesion in this second mode is caused by nearly perfectly smooth bond between oxide skin and substrate around the perimeter of the drops. This bond is so smooth because it is formed through rapid oxidation of a temporary bare liquid metal-substrate contact.

DESIGN AND CHARACTERIZATION OF SIGNLE CHANNEL TWO-LIQUID CAPACITOR

Although improved understanding of the fundamental mechanisms governing wetting and adhesion of gallium-based liquid metals enable fabrication of smaller liquid metal filled microchannels with higher areal density, the required serpentine geometry of resistive sensors remains quite complex. Motivated by simple scaling arguments presented in the introduction chapter, this chapter explores the concept of a capacitor composed of two liquid metal electrodes separated by a liquid dielectric material within a single straight cylindrical microchannel (see schematic in Figure 1.1b).

In this chapter, the experimental setup consisting of two GaInSn filled tubes submerged in a dielectric liquid bath is introduced; the effects of the cylindrical electrode geometry including the diameter, spacing, and meniscus shape as well as the dielectric constant of the insulating liquid and the presence of tubing on the overall system's capacitance are quantified; simulations of various systems are shown as well. (S. Liu et al., 2015)

Experimental setup

In order to systematically study the effects of geometry on capacitance of the two-liquid system without the hassle of fabricating multiple devices, the simple testing setup shown in Figure 3.1 and Figure 3.3a was developed. This system consists of two GaInSn filled thin-walled PVC tubes ($\varepsilon \sim 3.2$) that are aligned along the same axis and submerged in a dielectric liquid bath. The tubes were filled with GaInSn up to their open ends, which were arranged to face each other. The separation distance between the two tubes was adjusted using a micrometer and the shape of each of the liquid

metal–liquid dielectric interfaces was controlled by applying pressure to the syringes that were used to supply the liquid metal. Further details of the setup fabrication are described in the Experimental Chapter.

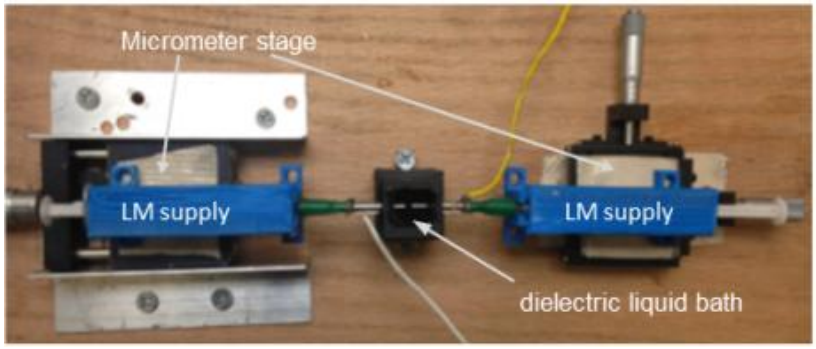

Figure 3.1 Picture of the experimental two-tube and dielectric "bath" setup.

Two liquid capacitor simulation

A 2D axisymmetric simulation of the electric field around the different geometries of the two liquid capacitor with and without tube was performed using the Electrostatic module in COMSOL Multiphysics 5.0 modelling software. The end-to-end facing 1 mm, 1.6 mm, and 2 mm liquid metal rods with length of ~1 cm were surrounded by a 0.2 to 1 mm thick PCV (ε~3.2) or PDMS (ε~2.8) tubing a 2 cm tall and 1.5 cm radius 'cylinder' of region with adjustable dielectric constant (i.e. water, glycerol, silicone oil, or air). The overall domain size was increased until its value no longer affected the simulated capacitance values. Free triangular mesh with "finer" size was used to discretize the simulation domain. This mesh size was sufficiently small to provide a mesh independent solution. For boundary conditions, the outer surface of the upper liquid metal cylinder was set to "terminal", while the lower one was set to "ground". To test different geometrical arrangements (e.g. effect of presence of tubing), the dielectric constant of the different regions was adjusted.

Figure 3.2 shows example geometry, mesh, and entire potential field distribution resulting from the simulation.

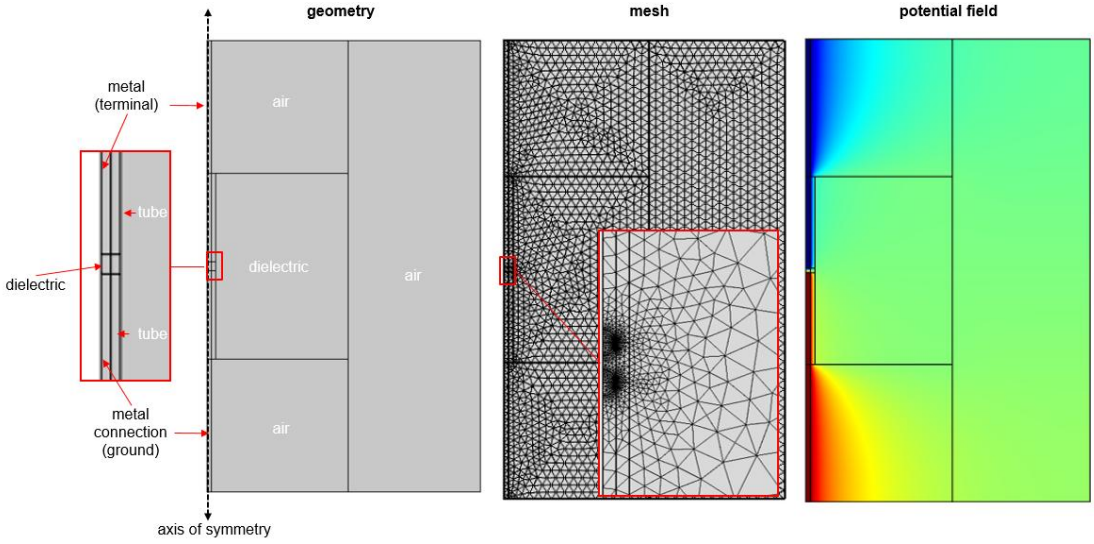

Figure 3.2 Example geometry, mesh, and potential field distribution resulting from the simulation.

Effects of geometry and dielectric liquid on capacitance of the two-liquid system

The capacitance of a system depends on the geometry of the conductors and the insulating materials in between. In this work, using a liquid insulator instead of a solid elastomer enables tailoring of the system's capacitance by selecting high or low dielectric constant liquids. The effects of electrode geometry including the diameter, separation distance, meniscus shape and oxide shell formation on the overall system's capacitance can also be quantified.

Selection of dielectric liquids. In electromagnetism, permittivity is a measure of how an electric field is affected by a dielectric medium, or how easily a dielectric polarizes in response to an electric field. ("Permittivity," 2015) The relative permittivity of a material is its dielectric permittivity scaled by the permittivity of

vacuum, which is commonly known as dielectric constant. ("Relative permittivity," 2015)

Since parallel plate capacitance is proportional to both dielectric constant of the insulating liquids, a decrease in the required length of the parallel channels, and with that of the sensor footprint, should be achievable by increasing the dielectric constant of the insulator material. Thus solid elastomer is replaced by high dielectric constant liquids such as pure water and glycerol. As a reference, silicone oil served as a control to mimic the PDMS elastomer. Relative permittivities (dielectric constant) of these materials at room temperature are shown below ("Relative permittivity," 2015):

Table 3.1

Relative permittivities (dielectric constant) of some materials at room temperature under 1 kHz

Material	$\boldsymbol{\varepsilon}$
Vacuum	1 (by definition)
Air	1.00058986 ± 0.00000050(Hector & Schultz, 1936) (at STP, for 0.9 MHz)
Pure water	80
Glycerol	42.5
Silicone oil	2.2-2.8

Effects of separation distance and dielectric liquid. First, the capacitance of two flat-ended cylindrical electrodes with diameters of 1 mm and 2 mm separated by 0.1 mm to 13.5 mm that were submerged in glycerol, water, and as reference, silicone oil was measured. The plots in Figure 3.3c and d show that by replacing silicone oil with glycerol and water the system's capacitance increases from ~1–1.5 pF to ~4–5 pF and ~6–7 pF for electrode separation distances below ~0.5 mm, respectively. This 3- to 5-fold capacitance increase is significantly smaller than the ~15 (40/2.8) to ~30 (80/2.8)

increase predicted by dielectric constant ratios described in the Introduction section. In addition, doubling of the electrode diameter (see Figure 3.3c and d) increases the measured capacitance by a factor of two, not four, as predicted by the basic parallel plate model.

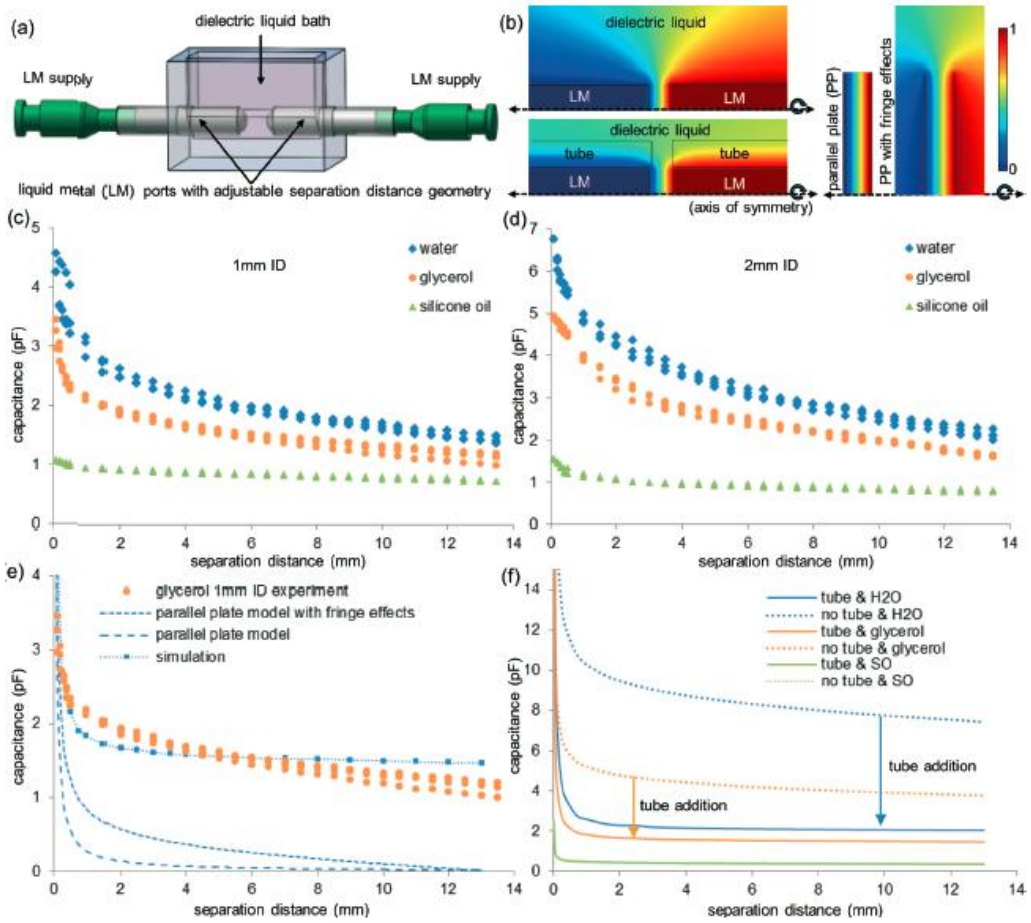

Figure 3.3 (a) Schematic of the setup used to characterize the capacitance of the liquid metal (LM)-liquid dielectric capacitor. (b) example of simulated potential fields around the capacitors consisting of flat-ended cylinders with and without tubing as well as parallel plates with and without electric fringe effects; (c-d) measured capacitance of two flat-ended cylindrical metal electrodes with diameters of (c) 1 mm and (d) 2 mm separated by silicone oil, glycerol and water; (e) comparison of experimentally measured, simulated, and calculated capacitance using a parallel plate model with and without fringe effects for two flat-ended cylindrical metal electrodes with 1 mm diameter separated by glycerol; and (f) comparison of simulated capacitance values for cylinders with and without tubing.

To explain these trends the experimental data were compared to simulations as well as theoretical predictions using the parallel plate model with and without fringe effects. The concept of fringe effect is an important phenomenon that needs to be explained here. Taking the capacitor formed by two parallel plates as an example, the electric field does not end abruptly at the edge of the plates. In practice an field outside of the that plates exists. This effect causes the real capacitance of the parallel plate capacitor to be larger than calculated by the formula. Examples of electric fields and potential fields distribution around the capacitors consisting of two parallel plates are illustrated in Figure 3.4.

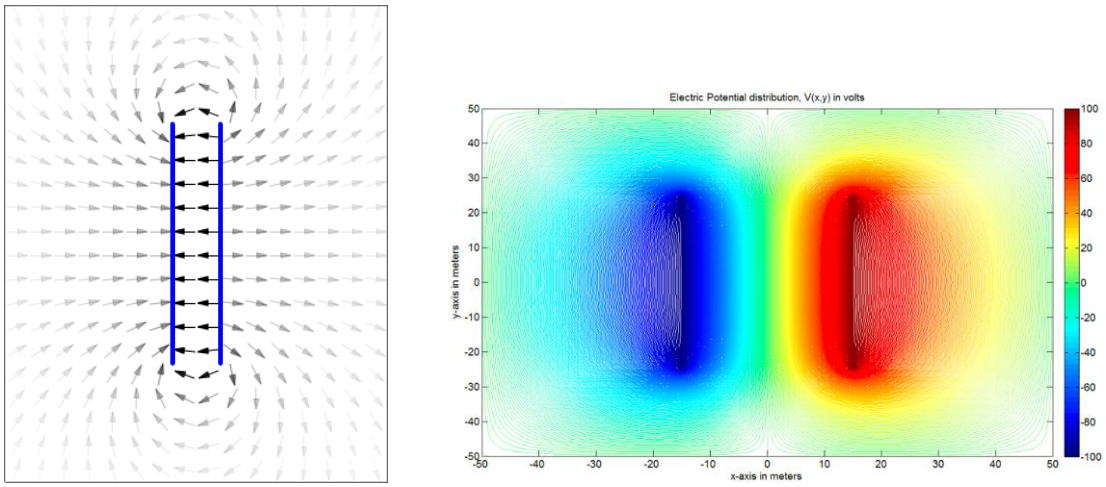

Figure 3.4 parallel plate capacitor fringe effects("Field in a Parallel-Plate Capacitor," n.d.; "Electric Field of a Parallel Plate capacitor using 2D Poisson Equation - File Exchange - MATLAB Central," n.d.)

For theoretical predictions, the analytical model derived by Landau et (Landau & Landau, 1984) that takes into account the electrical field fringe effects around the edges of the two electrodes (but not along the cylinder) was used:

$$C = \varepsilon_0 \varepsilon[(\frac{\pi r^2}{d} + r ln\left(\frac{16\pi r}{d} - 1\right)] \quad (3.1)$$

where r is the electrode radius. The plot in Figure 3.3e compares typical measured capacitance (in this case, 1 mm diameter electrodes wrapped in 0.5 mm thick tubing

separated by glycerol) as a function of separation distance to the simulation and analytical predictions. For small separation distances, the experimentally measured capacitance decreased proportionally to 1/d, in agreement with the parallel plate model scaling. However, when the separation distance was greater than ~1 mm, the measured capacitance values exceeded those predicted by either of the models by two to three times. In contrast, the simulation results, which capture the effects of the electrical field along the cylinders as well as the presence of the tube and the dielectric liquid outside the separation gap, match the experimental data well (see Appendix C for more simulation results). The simulation results in Figure 3.3f also show that the addition of tubing around the liquid metal electrodes results in a large decrease in the system's capacitance. Without the tubing, the switch from silicone oil to glycerol and water for 1 mm ID cylinders separated by 10 mm increases the capacitance from 0.37 pF to 3.93 pF and 7.76 pF, respectively. This corresponds to ~11- and ~21-fold capacitance increases related to the dielectric liquid change. The ~30% discrepancies between these values and those predicted from dielectric constant scaling likely stem from the finite dielectric bath volume in the simulations, which were designed to represent the experimental "bath" system. The presence of tubing, however, does not account for the capacitance scaling with the radius of the cylinders, not their end-areas. In particular, according to the simulations, increase in two "tube-less" metal cylinder diameters separated by 10 mm from 1 mm to 2 mm in silicone oil, glycerol, and water increases the capacitance by ~2.2(7.9/3.7), ~2.5(8.6/3.4), and ~2.2(16.9/7.8), respectively. This confirms strong influence of the electric field fringe effects along the tube as well as outside the electrode separation area, the latter of which scale with the radius of the electrode according to eq (3.1).

Effect of the liquid–liquid interface shape. Next the effect of curvature of the liquid metal–liquid dielectric interfaces on the system's capacitance was investigated. Quantification of this effect is particularly relevant to the single channel two-liquid capacitive strain sensor (gallium-based liquid metals embedded in PDMS) because a meniscus is likely to form at the liquids' interface due to the large difference between their surface tensions. (Thelen et al., 2012) The capacitance of electrodes with two types of menisci shown in Figure 3.5a was measured. The geometry of the menisci approached that of spherical-caps with liquid metal tube contact angles (θ) of ~55–60 ° and ~90–100 °, as defined from the line connecting the edges of the tube. The capacitance of the two hemisphere-ended cylindrical electrode system with and without tubing with $\theta = 90°$ as well as two spheres (see Figure 3.5b) was also simulated. The results are presented in Figure 3.5c and d in terms of meniscus tip-to-meniscus tip separation distance, while data in terms of meniscus base-to-meniscus base (i.e. end-of tube to end-of-tube) separation distance are illustrated in Figure 3.5e and f. The tip-to-tip distance was decreased until the electrodes touched and short-circuited by merging. Plots in Figure 3.5c to f show that the highest capacitance was measured for the systems consisting of two electrodes with menisci with θ~90–100 ° (i.e. about hemispherical), irrelevant of how the separation distance was specified. To theoretically take into account the meniscus shape, experimental data in Figure 3.5d is compared to to both simulations and series solution predicting the capacitance of two conducting spheres. The analytical solution to this problem was first derived by Maxwell using method of images (Maxwell & Thompson, 1892) and recently solved using bispherical coordinates by Gongora and Ley-Koo: (Mohammad R. Khan, Trlica, So, Valeri, & Dickey, 2014)

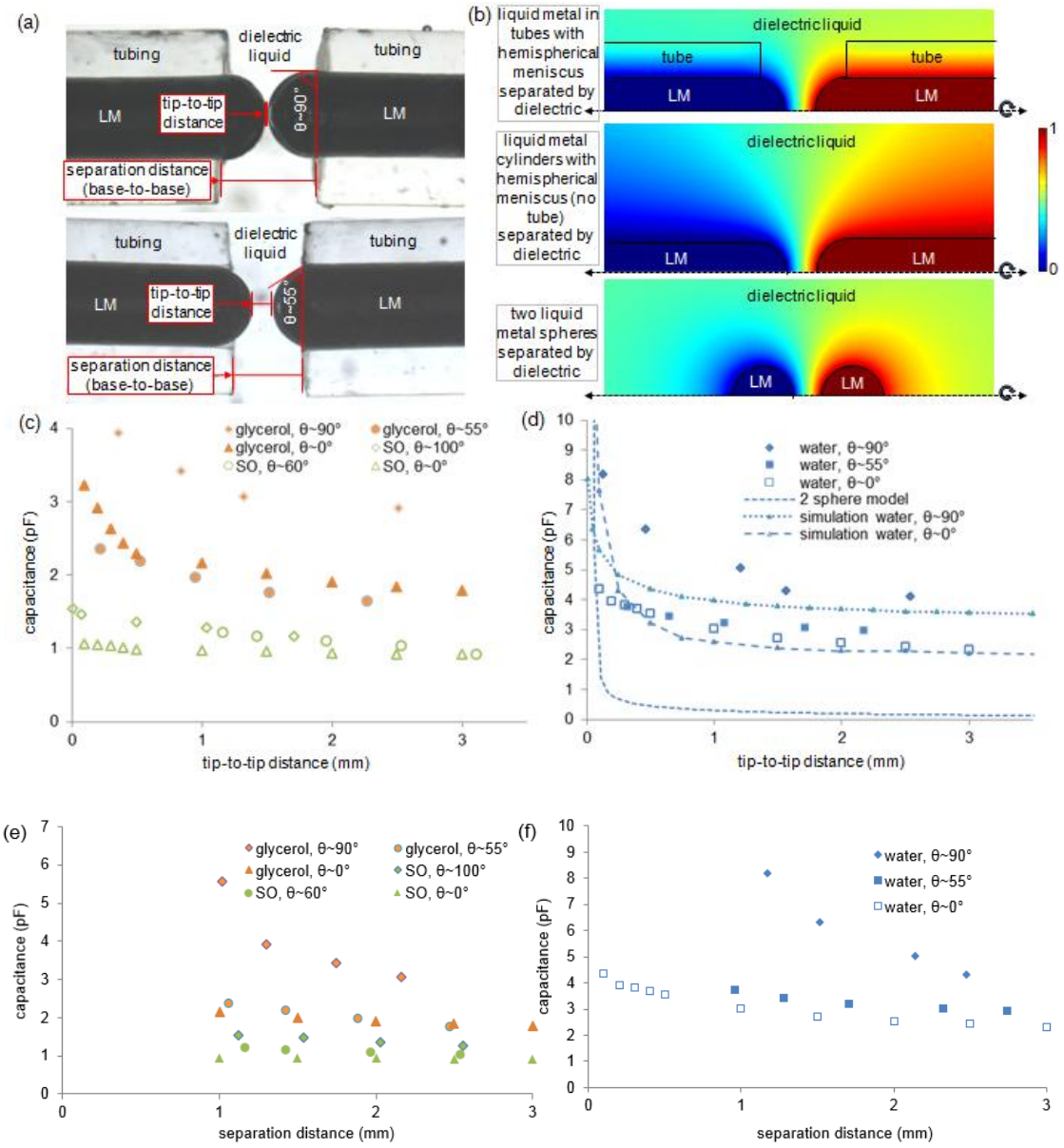

Figure 3.5 (a) Sample images of two-liquid capacitors with meniscus-ended electrodes with; θ ~ 60 °and θ ~ 90 °, (b) example of simulated potential fields around the capacitors consisting of hemisphere-ended cylinders with and without tubing as well as two spheres; (c-e) plot of measured capacitance of two symmetrical meniscus-ended electrodes and flat-ended electrodes (as a reference) separated by glycerol and silicone oil as a function of (c) tip-to-tip separation distances and (e) base-to-base separation distances; (d) comparison of experimentally measured and simulated capacitance for two symmetrical meniscus-ended electrodes and flat-ended electrodes separated by water as well as two spheres. (f) plot of measured capacitance of two hemisphere-ended and flat-ended cylinders as a function of base-to-base separation distances.

$$C = 4\pi\varepsilon_0\epsilon\frac{a}{2}\sum_{l=0}^{\infty}(l+\frac{1}{2})C_l(\cos h\eta_1)C_l(\cos h\eta_2)\,\mathrm{csch}[\left(l+\frac{1}{2}\right)(\eta_1-\eta_2)] \qquad (3.2)$$

In Eq (3.2) the two spheres positioned along the z-coordinate and are defined by a and η_i in the bi-spherical system with $r_i = a|\mathrm{csch}\,\eta_i|$ and $z_i = a\coth\eta_i$. The function $C_l(\cos h\eta_1)$ is defined as:

$$C_l(\cos h\eta_1) = \frac{1}{2^l N_l}(\mathrm{sech}\,\eta_1)^{\frac{1}{2}+l}\,{}_2\mathrm{F}_1\left(\frac{l}{2}+\frac{1}{4},\frac{l}{2}+\frac{3}{4},l+\frac{3}{2},sech^2\eta_1\right) \qquad (3.3)$$

In Eq (3.3) N_l are the normalization factors of the Legendre polynomials (N_0 = 1, N_1= 1, N_2 = 0.5, N_3 = 0.5, N_4 = 0.125, N_5 =0.125 etc.) and ${}_2\mathrm{F}_1$ is the hypergeometric function. Unfortunately, as shown in Figure 3.4b, the two-sphere model does not capture well the potential field distribution outside of the two-electrode separation gap and along the cylinders (with and without tubing). Consequently, the analytical model significantly under-predicts the capacitance. However, as in the case of flat-ended cylinders, the simulated values match the experimental values reasonably well (see Figure 3.5d). As observed in the experiments, the simulated capacitance of the hemisphere-ended cylinder system exceeds that of the flat-ended cylinder system for separation distances greater than ~0.1 mm. This effect likely stems from combination of the electric field distribution and larger interfacial "cap" area of the hemisphere ($2\pi r^2$ vs. πr^2).

Effect of the oxide shell. Next, the effect of formation of the gallium oxide skin on the system capacitance was investigated. This insulating few nanometer thick skin rapidly forms at the interface between the liquid metal and all studied dielectrics due to high solubility of oxygen in the dielectric liquids as well as its high permeability through PDMS. (Doudrick et al., 2014; Thelen et al., 2012) The effect of oxide skin growth was quantified using the setup shown in image in Figure 3.6. Just prior to start of the experiment, the original oxide skin formed at the two liquid interface was

removed with tweezers. Its removal and subsequent regrowth was confirmed visually, with the bare liquid metal having reflective “shinny” surface and the regrown oxide appearing as “dull” gray. (Doudrick et al., 2014) Because removal of the oxide skin at two liquid metal terminals could not be achieved simultaneously, one the liquid metal ports was replaced with a small metal plate. After oxide skin was removed, the capacitance values were recorded for 10 minutes in an interval of 10 seconds. The results plotted in Figure 3.5 show that the capacitance remains constant for the entire measured period for all dielectric liquids, indicating that presence of the oxide skin does not affect the capacitance.

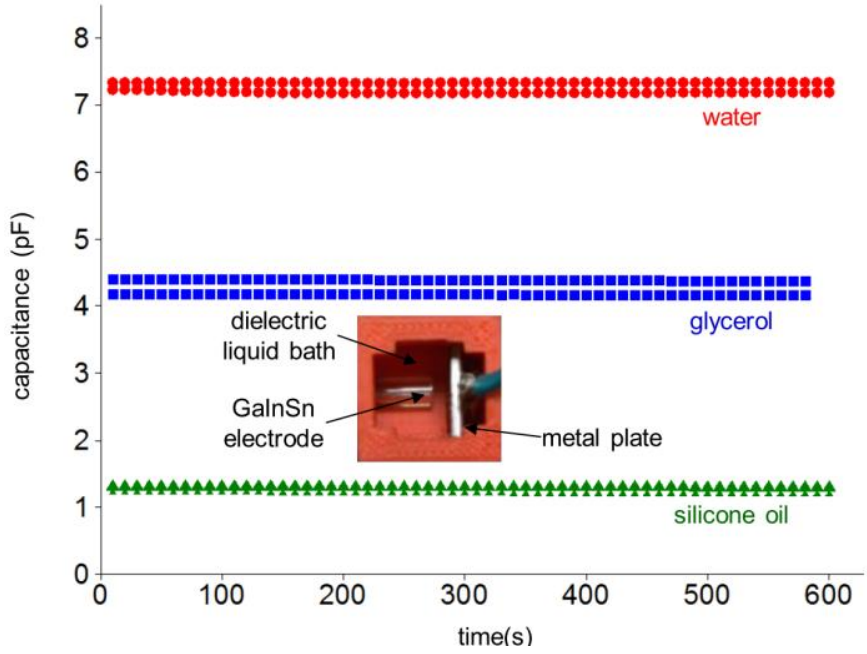

Figure 3.6 Effect of oxide skin growth at the liquid-liquid interface on the system’s capacitance.

SINGLE CHANNEL TWO-LIQUID CAPACITIVE STRAIN SENSOR

The results presented in Chapter 3 show that a two-liquid capacitor can have C ~ 5–8 pF with a footprint of only 1–2 mm^2 (i.e. ~50-fold reduction compared to two channel capacitors). Motivated by these results, in this Chapter the viability of a single channel two-liquid capacitive strain sensor is explored.

Device fabrication procedure

This device differs from the experimental setup in the previous chapter in that the liquid metal electrodes and the liquid dielectric are encapsulated within a single channel as opposed to having two liquid metal filled tubes separated by a liquid dielectric bath. As shown in the schematic in Figure 4.1, the device was fabricated by casting elastomer solution over a 3D printed rectangular casing pierced by a horizontal stainless steel shaft. After thermal curing of the elastomer, two-open ended cylindrical channel was created by removing the casted elastomer from the mold and pulling out the steel shaft. Filling of this channel with liquid metal electrodes separated by the liquid dielectric was the primary challenge in fabricating the two-liquid capacitive strain sensor. In principle this could be achieved by altering the flow of the two liquids. However, flowing of silicone oil, glycerol, and water into the PDMS channel filled with GaInSn resulted in residual liquid metal patches adhering to the channel walls (see Figure 4.1c). In general, this can be attributed to the formation and resulting morphology of the gallium oxide shell–substrate interface. (Doudrick et al., 2014) To resolve this issue the PDMS channel was “lubricated” prior to flowing GaInSn with flow of the dielectric liquid, preventing residual GaInSn adhesion to the PDMS walls. This observation was also recently reported by Dickey's group. (Mohammad R. Khan et al., 2014) After lubricating the channel with the

dielectric material, liquid metal was injected via a small temporary vertical hole near the middle of the channel. Temporarily sealing of one of the channel ends enabled the liquid metal to push about half of the dielectric liquid out of the channel through the open-end. After sealing of the first vertical hole with PDMS, majority of the remaining liquid dielectric material was pushed out through the previously sealed end by liquid metal that was injected through a second temporary vertical hole made nearby the original one. The image in Figure 4.1d shows that this procedure avoids sticking of liquid metal to the walls and can be used to fabricate single channel GaInSn–glycerol–GaInSn and GaInSn–water–GaInSn junctions. Since the surface tension of glycerol (63 mN/m) and water (72 mN/m) is much smaller than that of GaInSn (718 mN/m), the liquid metal forms a convex or "bulging" hemispherical meniscus on both sides of the junctions.

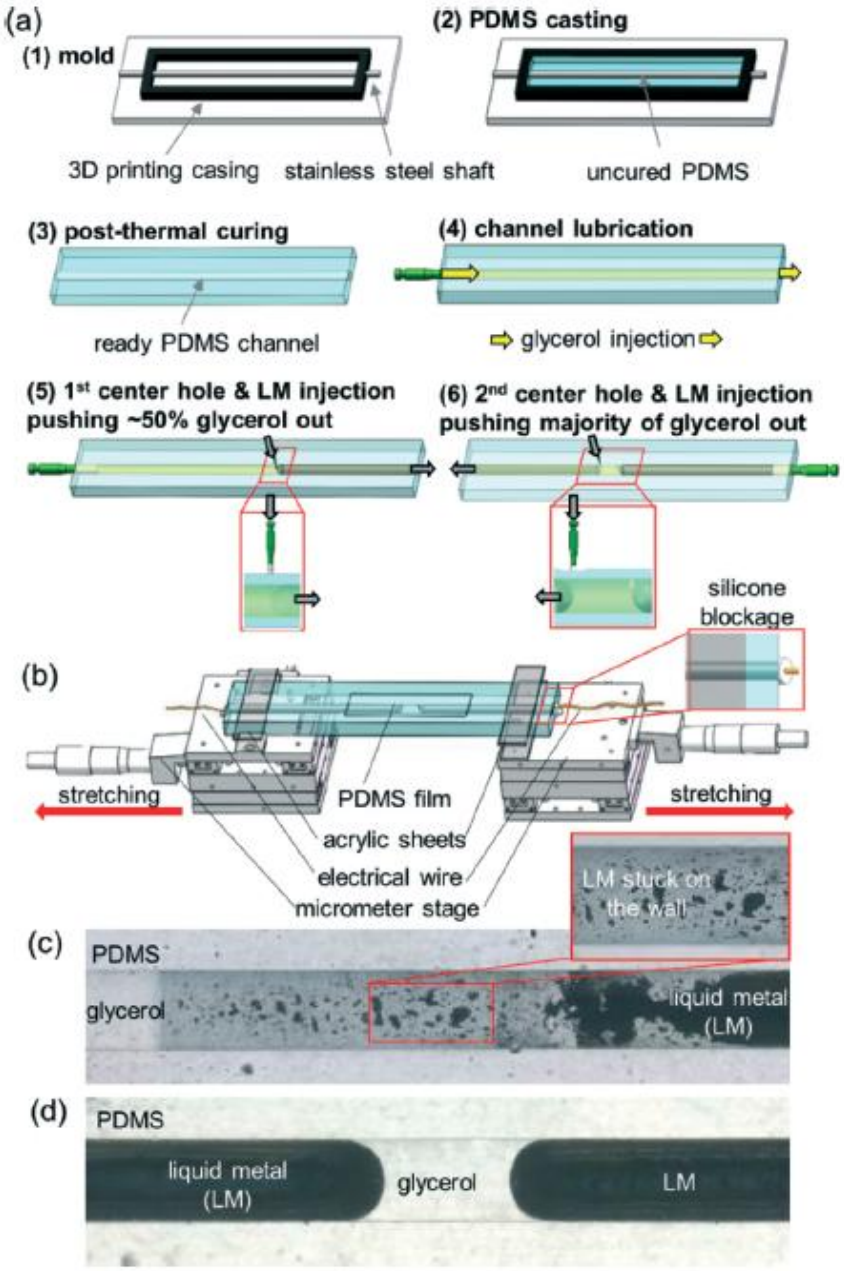

Figure 4.1 (a) Schematic of the single channel two-liquid capacitor fabrication procedure and its mounting in the (b) strain testing setup; (c) image showing residual liquid metal (LM) after it was partially pushed out with the glycerol flow; (d) image of the 16 mm diameter two-liquid capacitor fabricated using the procedure shown in (a).

Device performance

The described procedure could be used to repeatedly fabricate single channel two-liquid capacitors with glycerol and water as dielectric liquids. However, fabrication of

a complete two-liquid device that was stable under "static" conditions did not guarantee its stability during stretching. For example, the image in Figure 4.2a shows that during initial stages of stretching of the GaInSn–water–GaInSn capacitor, the liquid metal electrodes did not move gradually but "snapped" leaving behind residues on the PDMS walls. The sudden movement and residual GaInSn indicate that the oxide shell grew at the liquid metal–PDMS interface causing high adhesion. Consequently, its was found the use of water as dielectric liquid to be impractical and focused on capacitors filled with glycerol. Due to the manual nature of the current fabrication process the electrode-to-electrode separation distance was difficult to control. The minimal meniscus tip-to-tip distance that we were able to fabricate using this procedure was ~2.3 mm. This system had an unstrained capacitance (C0) of 1.1 pF with a footprint of about 3 mm^2. We observed that the separation distance between the two electrodes can be reduced by compressing the other edges of the PDMS channels filled with liquid metal. This forced some of the glycerol stored in between the electrodes to flow into the thin annular gap along the PDMS and GaInSn interface. Using this approach it was possible to reduce the tip-to-tip electrode separation distance down to ~0.5 mm to ~1 mm, which produced a capacitance of ~2 pF to ~1.4 pF with a corresponding footprint of ~0.8 mm^2 to 1.6 mm^2. The capacitance of several glycerol–liquid metal capacitor channels was measured during stretching using the setup illustrated in Figure 4.1b. The plot in Figure 4.2b shows the response to the strain of devices that had as-fabricated electrode separation distance (s5 to s7) as well as several devices that had the electrode-separation distance reduced by compressing the outer edges of the PDMS channels (s1 to s4). All the devices had initial tip-to-tip separation distance in the range of ~0.5 mm to ~2.5 mm. Since the devices had

different initial electrode-to-electrode spacing, the data are presented in absolute terms. All the data follow the trends expected from Figure 3.3 and 3.5 as well as the simulation of the system. However, the geometry of the devices was altered by the stretching process in two ways. The first mode involved separation of the liquid metal electrode induced by the device stretching. The plot in Figure 4.2c shows stretching data for the "s2" device with corresponding images of the electrodes prior to and at the end of stretching. One of the electrodes in this device was separated into two parts through gradual necking as the device was stretched. Separation of the two electrodes created two capacitors in series, which significantly decreased the total capacitance. The role of the glycerol outflow from the electrode separation region is clearly highlighted in the second scenario illustrated in Figure 4.2d and e. Specifically, neither of the electrodes separated as the meniscus tip-to-tip distance was increased from ~2 mm to ~5 mm (with a stretch ratio of 5 mm/2 mm ~2.5). The plot in Figure 4.2e shows that during this part of stretching the PDMS length and the meniscus tip-to-tip distance were roughly proportional, with a stretch ratio of ~2 observed for PDMS. However, during the retraction the two distances did not decrease proportionally. In particular, the separation distance between the electrodes decreased below the starting ~2 mm to ~0.1 mm. Naturally, for this to occur the glycerol must have been displaced by the liquid metal. The decrease in the electrode separation distance increased the capacitance to ~2.5 pF from the starting C_0 ~ 1.4 pF. For this device, the glycerol outflow to the annual region only caused necking during the first stretching and retraction (back) cycle. The images in Figure 4.2e show that one of the electrodes finally separated during the second stretching cycle. We schematically show in Figure 4.2f that both electrode necking and breaking are due to the glycerol

outflow into the annual region between the electrode and PDMS. Once excess glycerol is stored within this region; stretching of the device induces radial stresses which force the glycerol to break up the liquid metal electrode.

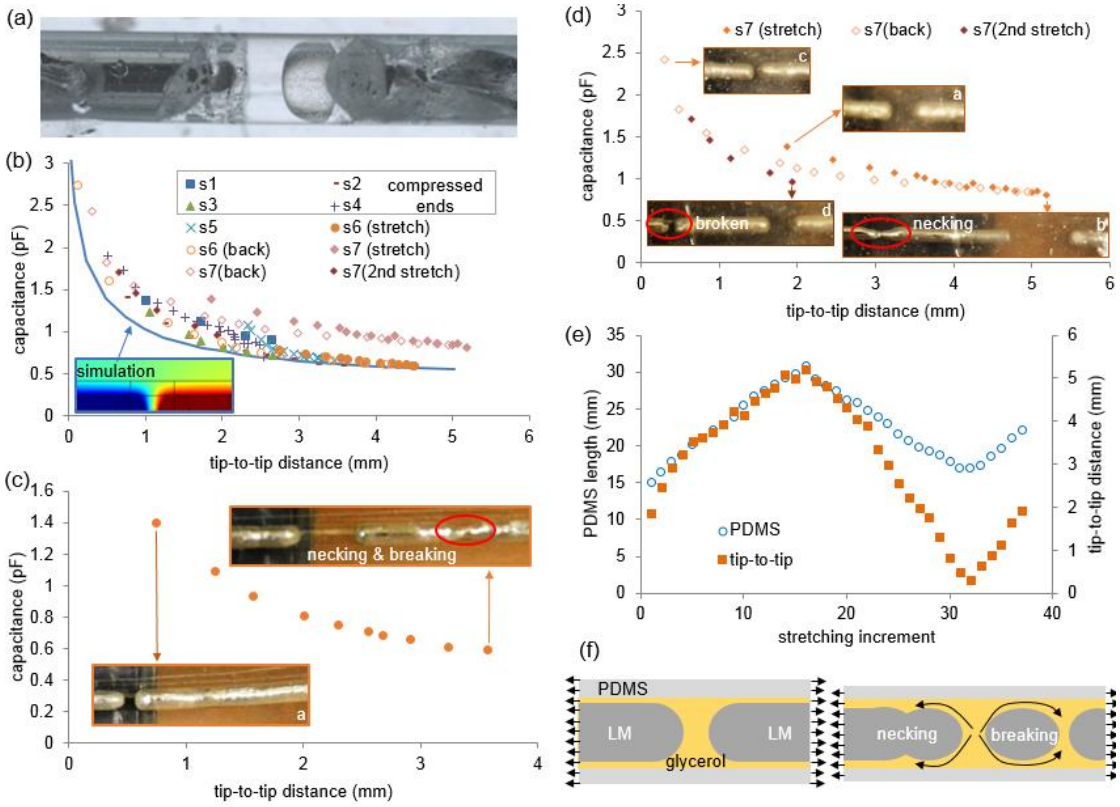

Figure 4.2 (a) Image of GaInSn-water-GaInSn device after stretching. (b-d) plots of measured capacitance as function of liquid metal menisci tip-to-tip separation distance for various GaInSn-glycerol-GaInSn devices: (b) all devices; (c) s2 device which had electrode separation distance reduced by "squeezing" or "compressing" the non-facing device ends, (d) s7 device whose non-facing device ends were not compressed, (e) comparison of PDMS device length and electrode menisci tip-to-tip separation distance during stretching, and (f) schematic of the glycerol device failure modes induced by glycerol outflow into the annual region separating PDMS and the electrodes.

EXPERIMENTAL SECTION

Materials

GaInSn with a composition of 68.5% Ga, 21.5% In, and 10% Sn was purchased from Rotometals. Water was purified to a resistivity of 18 MΩ cm using a Thermo Scientific™ Barnstead™ NanoPure™ system. Glycerol (≥99.5%, Sigma-Aldrich G9012) and silicone oil (viscosity, 100 cSt, Sigma-Aldrich, 378364) were used as the other two dielectric liquids. Elastomer substrates for capacitive strain sensors were fabricated by mixing elastomer base weighing 10 parts (around 15 g) and curing agent weighing 1 part (around 1.5 g) (Dow Corning, Sylguard 182, silicone elastomer kit). Four substrates were chosen to examine wetting properties of GaInSn including precleaned glass (Thermo Scientific, 2950-001), PDMS (Dow Corning, Sylguard 182, silicone elastomer kit), tungsten foil (Sigma-Aldrich 267538 99.9%), and 4,5-difluoro-2,2-bis-(trifluorormethyl)-1,3-dioxole, and PTFE polymer: tetrafluoroethylene (DBD) (DuPont, AF1600, 601S2100-6) and fluorinated solvent (3M,FC3283).

Substrate and Sample Preparation

Glass and tungsten substrates were clean by rinsing with acetone and water. The PDMS substrate was prepared by mixing the elastomer base and curing agents in a 10:1 ratio. The mixture was spread onto a glass slide and then cured at 100 ℃ for 20 min. Polytetrafluoroethylene (PTFE) was prepared using the procedure described by Park et al.(H. Park, Russell, & Park, 2010) Briefly, the PTFE precursor (i.e., DBD) was diluted with a fluorinated solvent to a concentration of 6 wt %, spin-coated onto a glass slide, and then annealed at 120 ℃ for 1 h.

Dynamic Contact Angle Measurements

The dynamic contact angles were measured using sample height and drop volume variation methods. In order to obtain a high magnification with a large depth of field and good lighting, the dynamic contact angle measurements were done using a custom 3D printed horizontal apparatus coupled with a high-magnification optical microscope (Zeiss Zoom Microscope Axial V16, 1.5× lens). To avoid effects of gravity, the GaInSn drop size was kept significantly below the capillary length (3.7 mm). The setup consisted of a 10 μL syringe (Hamilton 7635-01, 22 gauge blunt 9.52 mm needle), a 3D printed syringe holder with guides for the syringe plunger, a 90° aluminum substrate holder, and a micrometer X−Y−Z motion control stage (see schematic in Figure 2.4). Prior to contact angle measurements, the syringe was first cleaned with isopropanol and acetone and then loaded with GaInSn. The contact angles were measured using the angle tool plugin in ImageJ software. The reported values are averages and standard deviations of 6−10 measurements performed images from different stages of either the advancing or receding drop motion. Additional control experiment was carried out to ensure that major rupturing of the oxide shell did not occur during the height variation measurement; see discussion in Appendix A.

Two liquid metal filled tubes within a dielectric bath setup

The ABS system housing was 3D printed using Makerbot Replicator 2× and filled with dielectric liquids. The housing had two ports for passing liquid metal channels made of 1 mm or 2 mm internal diameter (ID) Masterkleer PVC tubing (Mcmaster-Carr), which was connected to 1 mL plastic syringes (Mcmaster-Carr) with corresponding 0.8 mm or 1.7 mm ID and 1.26 cm length blunt tip dispensing needles (Mcmaster-Carr). The spacing between the ends of the liquid metal tubes was adjusted

using two micro-positioning stages (Deltron, 1201-XYZ) attached to the 3D printed syringe holders using adhesive tape. For all of the tests, we used 889B Bench LCR/ESR Meter to measure capacitance and dissipation factors at a frequency of 200 kHz and a voltage of 1 V in parallel mode. A home-made faraday cage was used to shield the devices from electromagnetic interference during measurements. To make electrical contacts, copper wires were soldered onto the conductive syringe needles. The stray capacitance of the system was quantified with just air at different levels of relative humidity as well as long electrode separation distances. The results presented in Appendix A.1 show that the stray capacitance was negligible.

To study the effect of the liquid metal meniscus shape on device capacitance, the bottom of the 3D printed housing was replaced by a pre-cleaned glass slide (Thermo Scientific). This modification enabled detailed visualization of the meniscus shape using transmitted light in a Zeiss Axio-Zoom V 16 microscope fitted with a Z 1.5×/0 37 FWD 30 mm lens. Menisci with two different spherical-cap shapes characterized by the metal-tube contact angles of ~60 ° and ~90 ° were fabricated by manually adjusting the syringes. The capacitance was measured off-site within the faraday cage after the geometry of the device was adjusted under the microscope.

Single channel two-liquid capacitor fabrication procedure

The channel was fabricated within a single step by casting the elastomer solution over a 3D printing rectangular casing pierced by a 1.6 mm diameter and 7.6 cm length stainless steel shaft (McMaster-Carr). The PDMS solution was mixed in Petri dishes and poured into the mold. Before curing the PDMS mixture was degassed for around 30 minutes until all air bubbles escaped. Subsequently, the casted elastomer was heated for 1.5 h at 85 ℃ on a hot plate. After curing, the cast was removed from the

mold, with the steel shaft simply pulled out to create the two-open-ended channel with circular cross-section. To fabricate the three-sandwiched liquid layout while preventing the liquid metal from adhering to the wall of the channel during stretching, we injected the dielectric liquids first in order to lubricate the channel. Next, we blocked one side of the channel with a syringe and injected GaInSn by piercing a hole through the top of the PDMS into the channel using a 1 mL syringe with 1.26 cm long 0.03 cm ID blunt tip dispensing needles (McMaster-Carr, 75165A686). As a result the insulating liquid was ejected from the free side of the channel. To prevent leakage during testing, we sealed the vertical hole with a few drops of the uncured elastomer to the hole on the top and let it cure naturally without additional heating (to prevent hardening of the PDMS). After the first hole was sealed, another point located at a specified distance away from the first one was made and liquid metal was injected again to push out majority of the dielectric liquid from the channels. The result was a controlled amount of dielectric liquid separating the GaInSn. To finalize the device fabrication, wires were inserted into the ends of the channels.

PDMS sensor stretching experiments

The ends of the PDMS devices were mounted onto two micropositioning stages (Deltron, 1201-XYZ) by sandwiching them between flat acrylic “clamps”. For experiments involving the devices with “compressed” non-facing ends, the channel ends were fitted with a thin copper wire and sealed using silicone prior to mounting on the stage (thus clamping compressed the ends of the device). For testing of the non-squeezed devices, the channel ends were sealed after clamping onto the stage. During each stretching step the device was photographed from a top-down view using a Nikon 3200 camera. The capacitance of the system without the PDMS channel

being filled with liquid metal electrodes (so wires, stages etc.) in air below 50% relative humidity was below 0.15 pF for PDMS with a length of ~2.7 cm.

CONCLUSIONS

At the beginning of the thesis, macroscale dynamic contact angle measurements were performed to acquire contact angle hysteresis and understand the fundamental mechanisms governing wetting and adhesion behaviours of gallium-based liquid metals. Because of the rapid oxidation of Ga-based liquid metals, an oxide shell forms over the liquid and dominates the drop−substrate interactions. Using nano- to macroscale experimentation, it was demonstrated that, depending on the formation process and resulting morphology of the liquid metal−substrate interface, GaInSn adhesion can occur in two modes. First, if the oxide shell is not ruptured as it makes contact with the substrate, only a solid−solid contact is established. The natural nanoscale and microscale topology of the oxide surface results in minimal adhesion between the liquid metal and most solids, regardless of substrate's surface energy or texture. Only viscoelastic and air permeable PDMS, which can readily fill the space in between the nano/microscale topological features of the oxide, had high adhesion to the unruptured oxide. (D. Kim, Lee, Choi, et al., 2013) In the second adhesion mode, the formation of the GaInSn−substrate interface involves rupturing of the original oxide skin. Thus, a composite interface including contact between the substrate and pieces of old oxide, bare liquid metal, and new oxide is formed. The new insight into the fundamental mechanisms governing GaInSn wetting and adhesion developed here may help to improve the spatial resolution of other liquid metal fabrication techniques.

Next, a novel concept for a capacitor consisting of a liquid dielectric material sandwiched in between two liquid metal electrodes within a single straight cylindrical

channel was introduced. First, simulations and a simple setup consisting of two liquid metal filled tubes submerged in a dielectric liquid bath was used to quantify the effects of the electrode geometry including the diameter, separation distance, meniscus shape, and oxide shell as well as the dielectric constant of the insulator liquid on the system's capacitance. It was demonstrated that by replacing silicone oil with glycerol and water a three- to five-fold increase in the system's capacitance can be achieved. This increase is substantial but not as large as expected based on the ratio of the dielectric constants of the insulator liquids. Using simulations it was shown that this effect is due to the presence of low dielectric constant tubing (PVC and PDMS). Using simulations we also demonstrated that electric fringe effects outside the separation gap and along the cylinder are responsible for the capacitance scaling with the radius of the electrodes and not their end areas. It was found that for all geometries the measured capacitance cannot be predicted by classical analytical models for parallel plate or two-sphere capacitors and that full system numerical simulation is required to adequately capture the electrical field distribution. With the optimal geometry composed of hemispherical menisci and minimal separation distance, it was found that glycerol and water systems with a capacitance of ~5 pF to ~8 pF and a footprint of only ~1–2 mm^2 are feasible.

In addition, the feasibility of using a two-liquid capacitor within a single PDMS channel for hyperelastic strain sensing was explored. Residual GaInSn adhesion to the channel walls was prevented by lubricating the PDMS channel with water or glycerol prior to liquid metal injection. This enabled fabrication of single-channel liquid metal capacitors separated by glycerol and water. Unfortunately, oxide regrowth at the GaInSn–PDMS interface in the presence of water rendered strain sensors with water

as the dielectric material impractical. In particular, when stretching, the liquid metal electrodes did not deform gradually but suddenly "snapped" leaving behind residual GaInSn on the PDMS walls. This behavior was not observed in glycerol devices, indicating persistent PDMS wall lubrication by this dielectric liquid. For glycerol devices fit within a 1.6 mm diameter channel, the minimal meniscus tip-to-tip distances that we achieved with and without compressing of the device's outer edges were ~0.5 mm and ~2.3 mm, corresponding to capacitance values of ~2 pF and ~1.1 pF with footprints of ~0.8 mm^2 and ~3 mm^2, respectively. Thus, it was demonstrated that a single PDMS channel two-liquid capacitor can have about a ~25-fold higher capacitance per sensor's base area as compared to the current winding two-channel capacitors (2 pF/0.8 mm^2 vs. ~10 pF/100 mm^2). However, further experiments revealed that the liquid metal electrode geometry was altered by stretching. In particular, pressure induced by the stretching caused the outflow of glycerol from the region separating the electrodes to the annual region between the electrode and the PDMS channel wall. As a result, necking and breaking of the liquid metal electrodes were observed. Thus, while enabling fabrication and facile movement of the liquid metal electrodes, the presence of the "lubricating" glycerol also causes failure of the two-liquid capacitor.

This work illustrates that single channel two-liquid capacitors could provide a ~25 times more compact alternative to the current capacitive liquid metal strain sensors. However, application of the two-liquid capacitor to strain sensing is limited by glycerol–liquid metal fluid dynamics induced by stretching. Its noted that this does not represent a fundamental barrier, but rather a problem that could be resolved by an alternative fabrication procedure or altered design. Possible alternative designs could

include modification of the channel wall surface to reduce GaInSn adhesion, (Doudrick et al., 2014; Rebecca K. Kramer, Boley, et al., 2013; D. Kim, Lee, Choi, et al., 2013; G. Li et al., 2014) an alternative channel filling procedure (So & Dickey, 2011) or a hybrid approach between the single channel design and multichannel design recently introduced by Ota et al. (Ota et al., 2014) Other possibilities are to include an "overflow" region for the glycerol squeezed out of the center region or use its own oxide skin as channel to flow liquids in.

REFERENCES

Adhesion. (2015, January 31). In *Wikipedia, the free encyclopedia*. Retrieved from http://en.wikipedia.org/w/index.php?title=Adhesion&oldid=642678801

Antoniou, N., Rykaczewski, K., & Uchic, M. D. (2014). In situ FIB-SEM characterization and manipulation methods. *MRS Bulletin*, *39*(04), 347–352. http://doi.org/10.1557/mrs.2014.58

Benz, M., Rosenberg, K. J., Kramer, E. J., & Israelachvili, J. N. (2006). The Deformation and Adhesion of Randomly Rough and Patterned Surfaces. *The Journal of Physical Chemistry B*, *110*(24), 11884–11893. http://doi.org/10.1021/jp0602880

Boley, J. W., White, E. L., Chiu, G. T.-C., & Kramer, R. K. (2014). Direct Writing of Gallium-Indium Alloy for Stretchable Electronics. *Advanced Functional Materials*, *24*(23), 3501–3507. http://doi.org/10.1002/adfm.201303220

Cao, A., Yuen, P., & Lin, L. (2007). Microrelays With Bidirectional Electrothermal Electromagnetic Actuators and Liquid Metal Wetted Contacts. *Journal of Microelectromechanical Systems*, *16*(3), 700–708. http://doi.org/10.1109/JMEMS.2007.893520

Cheng, S., Rydberg, A., Hjort, K., & Wu, Z. (2009). Liquid metal stretchable unbalanced loop antenna. *Applied Physics Letters*, *94*(14), 144103. http://doi.org/10.1063/1.3114381

Cheng, S., & Wu, Z. (2010). Microfluidic stretchable RF electronics. *Lab on a Chip*, *10*(23), 3227–3234. http://doi.org/10.1039/C005159D

Cheng, S., & Wu, Z. (2011). A Microfluidic, Reversibly Stretchable, Large-Area Wireless Strain Sensor. *Advanced Functional Materials*, *21*(12), 2282–2290. http://doi.org/10.1002/adfm.201002508

Cheng, S., & Wu, Z. (2012). Microfluidic electronics. *Lab on a Chip*, *12*(16), 2782. http://doi.org/10.1039/c2lc21176a

Cheng, S., Wu, Z., Hallbjorner, P., Hjort, K., & Rydberg, A. (2009). Foldable and Stretchable Liquid Metal Planar Inverted Cone Antenna. *IEEE Transactions on Antennas and Propagation*, *57*(12), 3765–3771. http://doi.org/10.1109/TAP.2009.2024560

Chibowski, E., & Terpilowski, K. (2008). Surface free energy of sulfur--revisited I. Yellow and orange samples solidified against glass surface. *Journal of Colloid*

and Interface Science, *319*(2), 505–513. http://doi.org/10.1016/j.jcis.2007.10.059

Chow, T. S. (1998). Wetting of rough surfaces. *Journal of Physics: Condensed Matter*, *10*(27), L445–L451. http://doi.org/10.1088/0953-8984/10/27/001

Contact angle. (2015, January 23). In *Wikipedia, the free encyclopedia*. Retrieved from http://en.wikipedia.org/w/index.php?title=Contact_angle&oldid=618859920

Contact Angles. (n.d.). Retrieved February 2, 2015, from http://chemwiki.ucdavis.edu/Physical_Chemistry/Physical_Properties_of_Matter/Bulk_Properties/Cohesive_And_Adhesive_Forces/Contact_Angles

Cumby, B. L., Hayes, G. J., Dickey, M. D., Justice, R. S., Tabor, C. E., & Heikenfeld, J. C. (2012). Reconfigurable liquid metal circuits by Laplace pressure shaping. *Applied Physics Letters*, *101*(17), 174102. http://doi.org/10.1063/1.4764020

Dickey, M. D. (2014). Emerging applications of liquid metals featuring surface oxides. *ACS Applied Materials & Interfaces*, *6*(21), 18369–18379. http://doi.org/10.1021/am5043017

Dickey, M. D., Chiechi, R. C., Larsen, R. J., Weiss, E. A., Weitz, D. A., & Whitesides, G. M. (2008). Eutectic Gallium-Indium (EGaIn): A Liquid Metal Alloy for the Formation of Stable Structures in Microchannels at Room Temperature. *Advanced Functional Materials*, *18*(7), 1097–1104. http://doi.org/10.1002/adfm.200701216

Doudrick, K., Liu, S., Mutunga, E. M., Klein, K. L., Damle, V., Varanasi, K. K., & Rykaczewski, K. (2014). Different Shades of Oxide: From Nanoscale Wetting Mechanisms to Contact Printing of Gallium-Based Liquid Metals. *Langmuir*, *30*(23), 6867–6877. http://doi.org/10.1021/la5012023

Dumke, M. F., Tombrello, T. A., Weller, R. A., Housley, R. M., & Cirlin, E. H. (1983). Sputtering of the gallium-indium eutectic alloy in the liquid phase. *Surface Science*, *124*(2–3), 407–422. http://doi.org/10.1016/0039-6028(83)90800-2

D ZRNIC, D. S. S. (1969). On the resistivity and surface tension of the eutectic alloy of gallium and indium. *Journal of The Less Common Metals*, *18*(1), 67–68. http://doi.org/10.1016/0022-5088(69)90121-0

Electric Field of a Parallel Plate capacitor using 2D Poisson Equation - File Exchange - MATLAB Central. (n.d.). Retrieved April 3, 2015, from

http://www.mathworks.com/matlabcentral/fileexchange/file_infos/42773-electric-field-of-a-parallel-plate-capacitor-using-2d-poisson-equation

Fassler, A., & Majidi, C. (2013). 3D structures of liquid-phase GaIn alloy embedded in PDMS with freeze casting. *Lab on a Chip*, *13*(22), 4442–4450. http://doi.org/10.1039/C3LC50833A

Fassler, A., & Majidi, C. (2013). Soft-matter capacitors and inductors for hyperelastic strain sensing and stretchable electronics. *Smart Materials and Structures*, *22*(5), 055023. http://doi.org/10.1088/0964-1726/22/5/055023

Feng, X., Yang, B. D., Liu, Y., Wang, Y., Dagdeviren, C., Liu, Z., … Rogers, J. A. (2011). Stretchable Ferroelectric Nanoribbons with Wavy Configurations on Elastomeric Substrates. *ACS Nano*, *5*(4), 3326–3332. http://doi.org/10.1021/nn200477q

Field in a Parallel-Plate Capacitor. (n.d.). Retrieved February 6, 2015, from http://www.wiley.com/college/halliday/0470469080/simulations/sim31/sim31.html

Finkenauer, L. R., & Majidi, C. (2014). Complaint liquid metal electrodes for dielectric elastomer actuators. In Y. Bar-Cohen (Ed.), (p. 90563I). http://doi.org/10.1117/12.2049112

Galinstan - Wikipedia, the free encyclopedia. (n.d.). Retrieved January 24, 2015, from http://en.wikipedia.org/wiki/Galinstan

Gao, Y., Li, H., & Liu, J. (2012). Direct Writing of Flexible Electronics through Room Temperature Liquid Metal Ink. *PLoS ONE*, *7*(9), e45485. http://doi.org/10.1371/journal.pone.0045485

Gao, Y., Li, H., & Liu, J. (2013). Directly Writing Resistor, Inductor and Capacitor to Composite Functional Circuits: A Super-Simple Way for Alternative Electronics. *PLoS ONE*, *8*(8), e69761. http://doi.org/10.1371/journal.pone.0069761

Gennes, P.-G. de, Brochard-Wyart, F., & Quere, D. (2004). *Capillarity and Wetting Phenomena: Drops, Bubbles, Pearls, Waves*. Springer Science & Business Media.

Haiyan Li, J. L. (n.d.). Revolutionizing heat transport enhancement with liquid metals: Proposal of a new industry of water-free heat exchangers, *5*(1), 20–42. http://doi.org/10.1007/s11708-011-0139-9

Hayes, G. J., Desai, S. C., Liu, Y., Annamaa, P., Lazzi, G., & Dickey, M. D. (2014). Microfluidic coaxial transmission line and phase shifter. *Microwave and Optical Technology Letters*, *56*(6), 1459–1462. http://doi.org/10.1002/mop.28327

Hector, L. G., & Schultz, H. L. (1936). The Dielectric Constant of Air at Radiofrequencies. *Physics*, *7*(4), 133. http://doi.org/10.1063/1.1745374

Israelachvili, J. N. (2011). Adhesion and Wetting Phenomena. In *Intermolecular and Surface Forces* (pp. 415–467). Elsevier. Retrieved from http://linkinghub.elsevier.com/retrieve/pii/B9780123919274100179

Jalali Mazlouman, S., Jiang, X. J., Mahanfar, A., Menon, C., & Vaughan, R. G. (2011). A Reconfigurable Patch Antenna Using Liquid Metal Embedded in a Silicone Substrate. *IEEE Transactions on Antennas and Propagation*, *59*(12), 4406–4412. http://doi.org/10.1109/TAP.2011.2165501

Jeong, S. H., Hagman, A., Hjort, K., Jobs, M., Sundqvist, J., & Wu, Z. (2012a). Liquid alloy printing of microfluidic stretchable electronics. *Lab on a Chip*, *12*(22), 4657–4664. http://doi.org/10.1039/c2lc40628d

Jeong, S. H., Hagman, A., Hjort, K., Jobs, M., Sundqvist, J., & Wu, Z. (2012b). Liquid alloy printing of microfluidic stretchable electronics. *Lab on a Chip*, *12*(22), 4657. http://doi.org/10.1039/c2lc40628d

Johnson, K. L., Kendall, K., & Roberts, A. D. (1971). Surface Energy and the Contact of Elastic Solids. *Proceedings of the Royal Society of London A: Mathematical, Physical and Engineering Sciences*, *324*(1558), 301–313. http://doi.org/10.1098/rspa.1971.0141

Khan, M. R., Hayes, G. J., Zhang, S., Dickey, M. D., & Lazzi, G. (2012). A Pressure Responsive Fluidic Microstrip Open Stub Resonator Using a Liquid Metal Alloy. *IEEE Microwave and Wireless Components Letters*, *22*(11), 577–579. http://doi.org/10.1109/LMWC.2012.2223754

Khan, M. R., Trlica, C., So, J.-H., Valeri, M., & Dickey, M. D. (2014). Influence of Water on the Interfacial Behavior of Gallium Liquid Metal Alloys. *ACS Applied Materials & Interfaces*, *6*(24), 22467–22473. http://doi.org/10.1021/am506496u

Kim, D.-H., & Rogers, J. A. (2008). Stretchable Electronics: Materials Strategies and Devices. *Advanced Materials*, *20*(24), 4887–4892. http://doi.org/10.1002/adma.200801788

Kim, D., Lee, D.-W., Choi, W., & Lee, J.-B. (2013). A Super-Lyophobic 3-D PDMS Channel as a Novel Microfluidic Platform to Manipulate Oxidized Galinstan. *Journal of Microelectromechanical Systems*, *22*(6), 1267–1275. http://doi.org/10.1109/JMEMS.2013.2278625

Kim, D., Lee, Y., Lee, D.-W., Choi, W., & Lee, J.-B. J. B. (2013). Hydrochloric acid-impregnated paper for liquid metal microfluidics. In *2013 Transducers Eurosensors XXVII: The 17th International Conference on Solid-State Sensors, Actuators and Microsystems (TRANSDUCERS EUROSENSORS XXVII)* (pp. 2620–2623). http://doi.org/10.1109/Transducers.2013.6627343

Kim, D., Thissen, P., Viner, G., Lee, D.-W., Choi, W., Chabal, Y. J., & Lee, J.-B. J. B. (2013). Recovery of nonwetting characteristics by surface modification of gallium-based liquid metal droplets using hydrochloric acid vapor. *ACS Applied Materials & Interfaces*, *5*(1), 179–185. http://doi.org/10.1021/am302357t

Kim, H.-J., Maleki, T., Wei, P., & Ziaie, B. (2009). A Biaxial Stretchable Interconnect With Liquid-Alloy-Covered Joints on Elastomeric Substrate. *Journal of Microelectromechanical Systems*, *18*(1), 138–146. http://doi.org/10.1109/JMEMS.2008.2011118

Kim, H.-J., Son, C., & Ziaie, B. (2008). A multiaxial stretchable interconnect using liquid-alloy-filled elastomeric microchannels. *Applied Physics Letters*, *92*(1), 011904. http://doi.org/10.1063/1.2829595

Knoblauch, M., Hibberd, J. M., Gray, J. C., & van Bel, A. J. (1999). A galinstan expansion femtosyringe for microinjection of eukaryotic organelles and prokaryotes. *Nature Biotechnology*, *17*(9), 906–909. http://doi.org/10.1038/12902

Koo, H.-J., So, J.-H., Dickey, M. D., & Velev, O. D. (2011). Towards All-Soft Matter Circuits: Prototypes of Quasi-Liquid Devices with Memristor Characteristics. *Advanced Materials*, *23*(31), 3559–3564. http://doi.org/10.1002/adma.201101257

Kramer, R. K., Boley, J. W., Stone, H. A., Weaver, J. C., & Wood, R. J. (2013). Effect of Microtextured Surface Topography on the Wetting Behavior of Eutectic Gallium–Indium Alloys. *Langmuir*, *30*(2), 533–539. http://doi.org/10.1021/la404356r

Kramer, R. K., Majidi, C., Sahai, R., & Wood, R. J. (2011). Soft curvature sensors for joint angle proprioception. In *2011 IEEE/RSJ International Conference on Intelligent Robots and Systems (IROS)* (pp. 1919–1926). http://doi.org/10.1109/IROS.2011.6094701

Kramer, R. K., Majidi, C., & Wood, R. J. (2011). Wearable tactile keypad with stretchable artificial skin. In *2011 IEEE International Conference on Robotics and Automation (ICRA)* (pp. 1103–1107). http://doi.org/10.1109/ICRA.2011.5980082

Kramer, R. K., Majidi, C., & Wood, R. J. (2013). Masked Deposition of Gallium-Indium Alloys for Liquid-Embedded Elastomer Conductors. *Advanced Functional Materials*, *23*(42), 5292–5296. http://doi.org/10.1002/adfm.201203589

Kubo, M., Li, X., Kim, C., Hashimoto, M., Wiley, B. J., Ham, D., & Whitesides, G. M. (2010). Stretchable Microfluidic Radiofrequency Antennas. *Advanced Materials*, *22*(25), 2749–2752. http://doi.org/10.1002/adma.200904201

Kunquan Ma, J. L. (2007). Liquid metal cooling in thermal management of computer chips. *Frontiers of Energy and Power Engineering in China*, *1*(4), 384–402. http://doi.org/10.1007/s11708-007-0057-3

Ladd, C., So, J.-H., Muth, J., & Dickey, M. D. (2013). 3D Printing of Free Standing Liquid Metal Microstructures. *Advanced Materials*, *25*(36), 5081–5085. http://doi.org/10.1002/adma.201301400

Lam, L. S., Hodes, M., & Enright, R. (2013). Analysis of Galinstan-Based Microgap Cooling Enhancement Using Structured Surfaces (p. V003T23A006). ASME. http://doi.org/10.1115/HT2013-17817

Landau, L. D., & Landau, L. D. (1984). *Electrodynamics of continuous media* (2nd ed., rev. and enl). Oxford [Oxfordshire] ; New York: Pergamon.

Li, G., Parmar, M., Kim, D., Lee, J.-B. J. B., & Lee, D.-W. (2014). PDMS based coplanar microfluidic channels for the surface reduction of oxidized Galinstan. *Lab on a Chip*, *14*(1), 200–209. http://doi.org/10.1039/c3lc50952d

Li, M., Yu, B., & Behdad, N. (2010). Liquid-Tunable Frequency Selective Surfaces. *IEEE Microwave and Wireless Components Letters*, *20*(8), 423–425. http://doi.org/10.1109/LMWC.2010.2049257

Liu, S., Sun, X., Hildreth, O. J., & Rykaczewski, K. (2015). Design and characterization of a single channel two-liquid capacitor and its application to hyperelastic strain sensing. *Lab Chip*. http://doi.org/10.1039/C4LC01341G

Liu, T., Sen, P., & Kim, C.-J. (2010). Characterization of liquid-metal Galinstan #x00AE; for droplet applications. In *2010 IEEE 23rd International Conference on Micro Electro Mechanical Systems (MEMS)* (pp. 560–563). http://doi.org/10.1109/MEMSYS.2010.5442440

Liu, T., Sen, P., & Kim, C.-J. (2012). Characterization of Nontoxic Liquid-Metal Alloy Galinstan for Applications in Microdevices. *Journal of Microelectromechanical Systems*, *21*(2), 443–450. http://doi.org/10.1109/JMEMS.2011.2174421

Majidi, C., Kramer, R., & Wood, R. J. (2011). A non-differential elastomer curvature sensor for softer-than-skin electronics. *Smart Materials and Structures*, *20*(10), 105017. http://doi.org/10.1088/0964-1726/20/10/105017

Ma, K.-Q., & Liu, J. (2007). Nano liquid-metal fluid as ultimate coolant. *Physics Letters A*, *361*(3), 252–256. http://doi.org/10.1016/j.physleta.2006.09.041

Maxwell, J. C., & Thompson, J. J. (1892). *A treatise on electricity and magnetism*. Clarendon.

Mercury (element). (2015, February 18). In *Wikipedia, the free encyclopedia*. Retrieved from http://en.wikipedia.org/w/index.php?title=Mercury_(element)&oldid=647642156

Microsoft Word - MSDS_Galinstan engl. 03_18_04 .doc - msds.pdf. (n.d.). Retrieved from http://www.rgmd.com/msds/msds.pdf

Morley, N. B., Burris, J., Cadwallader, L. C., & Nornberg, M. D. (2008). GaInSn usage in the research laboratory. *Review of Scientific Instruments*, *79*(5), 056107. http://doi.org/10.1063/1.2930813

Noda, K., Iwase, E., Matsumoto, K., & Shimoyama, I. (2010). Stretchable liquid tactile sensor for robot-joints. In *2010 IEEE International Conference on Robotics and Automation (ICRA)* (pp. 4212–4217). http://doi.org/10.1109/ROBOT.2010.5509301

Ota, H., Chen, K., Lin, Y., Kiriya, D., Shiraki, H., Yu, Z., … Javey, A. (2014). Highly deformable liquid-state heterojunction sensors. *Nature Communications*, *5*. http://doi.org/10.1038/ncomms6032

Paik, J. K., Kramer, R. K., & Wood, R. J. (2011). Stretchable circuits and sensors for robotic origami. In *2011 IEEE/RSJ International Conference on Intelligent Robots and Systems (IROS)* (pp. 414–420). http://doi.org/10.1109/IROS.2011.6094746

Palleau, E., Reece, S., Desai, S. C., Smith, M. E., & Dickey, M. D. (2013). Self-Healing Stretchable Wires for Reconfigurable Circuit Wiring and 3D Microfluidics. *Advanced Materials*, *25*(11), 1589–1592. http://doi.org/10.1002/adma.201203921

Parasitic capacitance. (2014, November 29). In *Wikipedia, the free encyclopedia*. Retrieved from http://en.wikipedia.org/w/index.php?title=Parasitic_capacitance&oldid=635899803

Park, H., Russell, T. P., & Park, S. (2010). Spatial control of dewetting: Highly ordered Teflon nanospheres. *Journal of Colloid and Interface Science*, *348*(2), 416–423. http://doi.org/10.1016/j.jcis.2010.05.011

Park, J., Wang, S., Li, M., Ahn, C., Hyun, J. K., Kim, D. S., … Jeon, S. (2012a). Three-dimensional nanonetworks for giant stretchability in dielectrics and conductors. *Nature Communications*, *3*, 916. http://doi.org/10.1038/ncomms1929

Park, J., Wang, S., Li, M., Ahn, C., Hyun, J. K., Kim, D. S., … Jeon, S. (2012b). Three-dimensional nanonetworks for giant stretchability in dielectrics and conductors. *Nature Communications*, *3*, 916. http://doi.org/10.1038/ncomms1929

Park, Y.-L., Majidi, C., Kramer, R., Bérard, P., & Wood, R. J. (2010). Hyperelastic pressure sensing with a liquid-embedded elastomer. *Journal of Micromechanics and Microengineering*, *20*(12), 125029. http://doi.org/10.1088/0960-1317/20/12/125029

Permittivity. (2015, January 31). In *Wikipedia, the free encyclopedia*. Retrieved from http://en.wikipedia.org/w/index.php?title=Permittivity&oldid=640954576

Ponce Wong, R. D., Posner, J. D., & Santos, V. J. (2012). Flexible microfluidic normal force sensor skin for tactile feedback. *Sensors and Actuators A: Physical*, *179*, 62–69. http://doi.org/10.1016/j.sna.2012.03.023

P. Sen, C.-J. K. (2009). Microscale Liquid-Metal Switches—A Review. *Industrial Electronics, IEEE Transactions on*, (4), 1314 – 1330. http://doi.org/10.1109/TIE.2008.2006954

Quéré, D. (2005). Non-sticking drops. *Reports on Progress in Physics*, *68*(11), 2495–2532. http://doi.org/10.1088/0034-4885/68/11/R01

Regan, M. J., Pershan, P. S., Magnussen, O. M., Ocko, B. M., Deutsch, M., & Berman, L. E. (1997). X-ray reflectivity studies of liquid metal and alloy surfaces. *Physical Review B*, *55*(23), 15874–15884. http://doi.org/10.1103/PhysRevB.55.15874

Regan, M. J., Tostmann, H., Pershan, P. S., Magnussen, O. M., DiMasi, E., Ocko, B. M., & Deutsch, M. (1997). X-ray study of the oxidation of liquid-gallium

surfaces. *Physical Review B*, *55*(16), 10786–10790. http://doi.org/10.1103/PhysRevB.55.10786

Relative permittivity. (2015, January 31). In *Wikipedia, the free encyclopedia*. Retrieved from http://en.wikipedia.org/w/index.php?title=Relative_permittivity&oldid=643333004

Rogers, J. A., Someya, T., & Huang, Y. (2010). Materials and Mechanics for Stretchable Electronics. *Science*, *327*(5973), 1603–1607. http://doi.org/10.1126/science.1182383

Scharmann, F., Cherkashinin, G., Breternitz, V., Knedlik, C., Hartung, G., Weber, T., & Schaefer, J. A. (2004). Viscosity effect on GaInSn studied by XPS. *Surface and Interface Analysis*, *36*(8), 981–985. http://doi.org/10.1002/sia.1817

Sivan, V., Tang, S.-Y., O'Mullane, A. P., Petersen, P., Eshtiaghi, N., Kalantar-zadeh, K., & Mitchell, A. (2013). Liquid Metal Marbles. *Advanced Functional Materials*, *23*(2), 144–152. http://doi.org/10.1002/adfm.201200837

So, J.-H., & Dickey, M. D. (2011). Inherently aligned microfluidic electrodes composed of liquid metal. *Lab on a Chip*, *11*(5), 905. http://doi.org/10.1039/c0lc00501k

So, J.-H., Thelen, J., Qusba, A., Hayes, G. J., Lazzi, G., & Dickey, M. D. (2009). Reversibly Deformable and Mechanically Tunable Fluidic Antennas. *Advanced Functional Materials*, *19*(22), 3632–3637. http://doi.org/10.1002/adfm.200900604

Spells, K. E. (1936). The determination of the viscosity of liquid gallium over an extended nrange of temperature. *Proceedings of the Physical Society*, *48*(2), 299. http://doi.org/10.1088/0959-5309/48/2/308

Tabatabai, A., Fassler, A., Usiak, C., & Majidi, C. (2013). Liquid-Phase Gallium–Indium Alloy Electronics with Microcontact Printing. *Langmuir*, *29*(20), 6194–6200. http://doi.org/10.1021/la401245d

Tadmor, R. (2004). Line Energy and the Relation between Advancing, Receding, and Young Contact Angles. *Langmuir*, *20*(18), 7659–7664. http://doi.org/10.1021/la049410h

Takadoum, J. (2013). *Materials and Surface Engineering in Tribology*. John Wiley & Sons.

Tang, S.-Y., Sivan, V., Khoshmanesh, K., O'Mullane, A. P., Tang, X., Gol, B., … Kalantar-zadeh, K. (2013). Electrochemically induced actuation of liquid metal marbles. *Nanoscale*, *5*(13), 5949–5957. http://doi.org/10.1039/c3nr00185g

Tang, S.-Y., Sivan, V., Petersen, P., Zhang, W., Morrison, P. D., Kalantar-zadeh, K., … Khoshmanesh, K. (2014). Liquid Metal Actuator for Inducing Chaotic Advection. *Advanced Functional Materials*, n/a–n/a. http://doi.org/10.1002/adfm.201400689

Tang, X., Tang, S.-Y., Sivan, V., Zhang, W., Mitchell, A., Kalantar-zadeh, K., & Khoshmanesh, K. (2013). Photochemically induced motion of liquid metal marbles. *Applied Physics Letters*, *103*(17), 174104. http://doi.org/10.1063/1.4826923

Thelen, J., Dickey, M. D., & Ward, T. (2012). A study of the production and reversible stability of EGaIn liquid metal microspheres using flow focusing. *Lab on a Chip*, *12*(20), 3961. http://doi.org/10.1039/c2lc40492c

Trlica, C., Parekh, D. P., Panich, L., Ladd, C., & Dickey, M. D. (2014). 3-D printing of liquid metals for stretchable and flexible conductors. In T. George, M. S. Islam, & A. K. Dutta (Eds.), (p. 90831D). http://doi.org/10.1117/12.2050212

Vetrovec, J., Litt, A. S., Copeland, D. A., Junghans, J., & Durkee, R. (2013). Liquid metal heat sink for high-power laser diodes (Vol. 8605, p. 86050E–86050E–7). http://doi.org/10.1117/12.2005357

V. Sivan, S. Y. T. (2012). Enhanced Electrochemical Heavy Metal Ion Sensor using Liquid Metal Marbles - Towards On-Chip Application, 213–214. http://doi.org/10.1109/COMMAD.2012.6472436

Wang, J., Liu, S., Vardeny, Z. V., & Nahata, A. (2012). Liquid metal-based plasmonics. *Optics Express*, *20*(3), 2346–2353. http://doi.org/10.1364/OE.20.002346

Wenjiang Shen, R. T. E. (2006). Electrostatically actuated metal-droplet microswitches integrated on CMOS chip. *Microelectromechanical Systems, Journal of*, (4), 879 – 889. http://doi.org/10.1109/JMEMS.2006.878877

Wetting. (2015, January 31). In *Wikipedia, the free encyclopedia*. Retrieved from http://en.wikipedia.org/w/index.php?title=Wetting&oldid=641877828

What is Stray Capacitance? (n.d.). Retrieved March 3, 2015, from http://www.learningaboutelectronics.com/Articles/What-is-stray-capacitance

WHITNEY, R. J. (1949). The measurement of changes in human limb-volume by means of a mercury-inrubber strain gauge. *The Journal of Physiology*, *109*(1-2), Proc, 5.

Wissman, J., Lu, T., & Majidi, C. (2013). Soft-matter electronics with stencil lithography. In *2013 IEEE SENSORS* (pp. 1–4). http://doi.org/10.1109/ICSENS.2013.6688217

Yang, C., Persson, B. N. J., Israelachvili, J., & Rosenberg, K. (2008). Contact mechanics with adhesion: Interfacial separation and contact area. *EPL (Europhysics Letters)*, *84*(4), 46004. http://doi.org/10.1209/0295-5075/84/46004

Yang, H., Lightner, C. R., & Dong, L. (2011). Light-Emitting Coaxial Nanofibers. *ACS Nano*, *6*(1), 622–628. http://doi.org/10.1021/nn204055t

Yang, Z., Deng, J., Chen, X., Ren, J., & Peng, H. (2013). A Highly Stretchable, Fiber-Shaped Supercapacitor. *Angewandte Chemie International Edition*, *52*(50), 13453–13457. http://doi.org/10.1002/anie.201307619

zafepress.php. (n.d.). Retrieved from http://www.biolinscientific.com/zafepress.php?url=%2Fpdf%2FAttension%2FTheory%20Notes%2FAT_TN_1_contactangle.pdf

Zappone, B., Rosenberg, K. J., & Israelachvili, J. (2007). Role of nanometer roughness on the adhesion and friction of a rough polymer surface and a molecularly smooth mica surface. *Tribology Letters*, *26*(3), 191–201. http://doi.org/10.1007/s11249-006-9172-y

Zhang, Q., Gao, Y., & Liu, J. (2013). Atomized Spraying of Liquid Metal Droplets on Desired Substrate Surfaces as a Generalized Way for Ubiquitous Printed Electronics. *arXiv:1311.2158 [cond-Mat, Physics:physics]*. Retrieved from http://arxiv.org/abs/1311.2158

Zhang, Q., & Liu, J. (2013). Nano liquid metal as an emerging functional material in energy management, conversion and storage. *Nano Energy*, *2*(5), 863–872. http://doi.org/10.1016/j.nanoen.2013.03.002

Zheng, Y., He, Z.-Z., Yang, J., & Liu, J. (2013). Fully Automatic Liquid Metal Printer towards Personal Electronics Manufacture. *arXiv:1312.0617 [cs]*. Retrieved from http://arxiv.org/abs/1312.0617

Zheng, Y., Zhang, Q., & Liu, J. (2013). Pervasive liquid metal direct writing electronics with roller-ball pen. *AIP Advances*, *3*(11), 112117. http://doi.org/10.1063/1.4832220

APPENDIX A

OXIDE SHELL MECHANICS AT DORP-SUBSTRATE INTERFACE DURING HEIGHT VARIATION METHOD

We conducted a simple experiment to verify that no major rupturing of the oxide shell has occurred during the height variation tests. We compared geometry of GaInSn drops before and after the test. Since, as shown in Figure A.1, the perimeter of the drop is nearly unchanged, it is unlikely that major rupturing, and with that new oxide surface formation, occurred.

Figure A GaInSn drop before and after height variation test. The perimeter of the drops is nearly identical before and after the test.

APPENDIX B

SYSTEM STRAY CAPACITANCE QUANTIFICATION

Stray capacitance is an undesired and unintended capacitance in a circuit that may affect performance of the whole system. When two conductors are close enough to each other, they are disturbed by each other's electric field and store opposite electric charges like a capacitor, which is referred to as stray capacitance or parasitic capacitance.("Parasitic capacitance," 2014, "What is Stray Capacitance?," n.d.)

Here, the stray capacitance of the system was quantified with just air at different levels of relative humidity as well as long electrode separation distances. The results presented in Figure A.2 show that the stray capacitance was negligible.

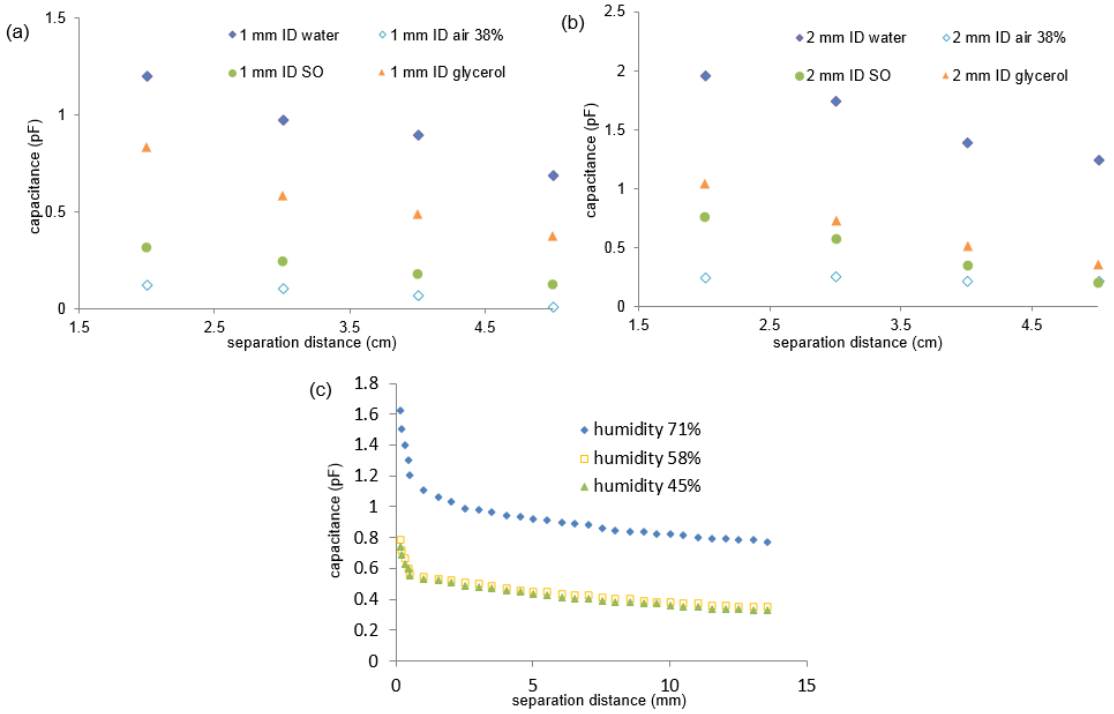

Figure B Capacitance measurements for two-liquid capacitors with flat-ended liquid metal electrodes separated by (a-b) large distances (2 to 5 cm) within different dielectric liquid baths and 38% relative humidity air for (a) 1 mm ID and (b) 2 mm ID tubes, and (c) distances (0.1 to 15 mm) within air at different relative humidity.

APPENDIX C

ADDITIONAL SIMULATION RESULTS

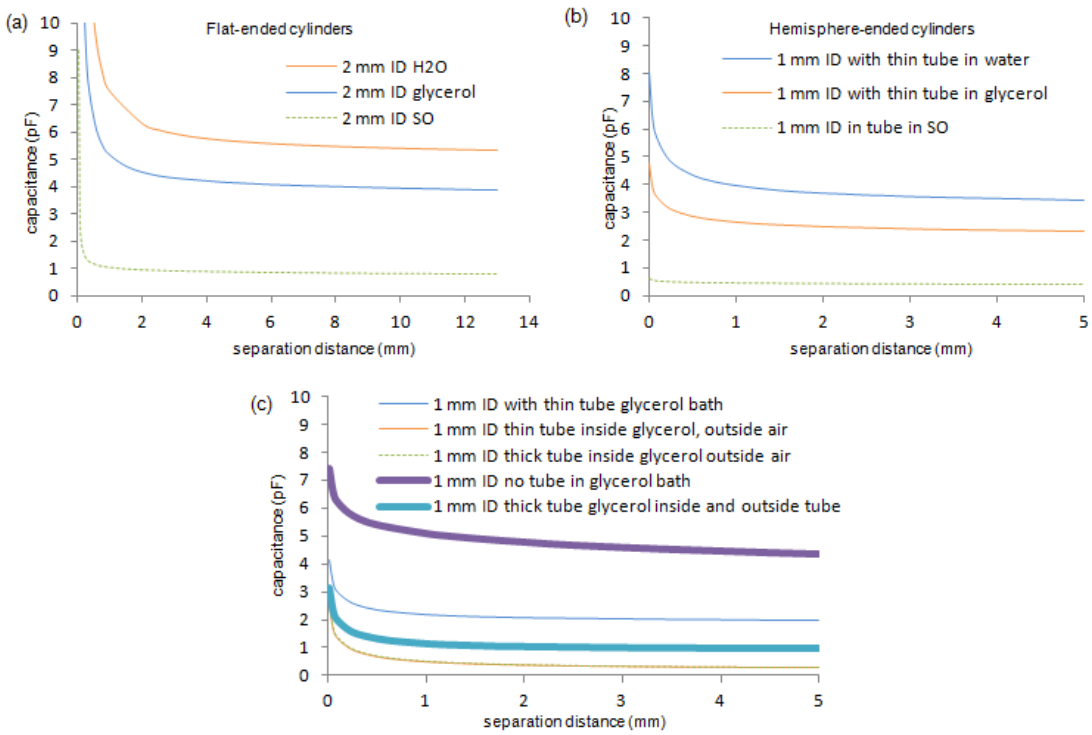

Figure C Additional simulation results: (a) for two-cylindrical flat ended 2mm ID electrodes in tube and (b) 1 mm hemisphere ended electrodes within a tube separated by different dielectric baths, and (c) various geometrical/material arrangements of the electrode system in (b).